SOURCE DATA TRANSPARENT PROCESS OPEN ACCESS

Queuosine-tRNA promotes sex-dependent learning and memory formation by maintaining codon-biased translation elongation speed

Cansu Cirzi[1,2] , Julia Dyckow[3,4] , Carine Legrand[1,5] , Johanna Schott[6,7] , Wei Guo[2,6,7] ,
Daniel Perez Hernandez[8] , Miharu Hisaoka[6,7] , Rosanna Parlato[9] , Claudia Pitzer[10] ,
Franciscus van der Hoeven[11] , Gunnar Dittmar[8,12] , Mark Helm[13] , Georg Stoecklin[2,6,7] ,
Lucas Schirmer[3,4,14] , Frank Lyko[1] & Francesca Tuorto[1,6,7,*]

Abstract

Queuosine (Q) is a modified nucleoside at the wobble position of specific tRNAs. In mammals, queuosinylation is facilitated by queuine uptake from the gut microbiota and is introduced into tRNA by the QTRT1-QTRT2 enzyme complex. By establishing a *Qtrt1* knockout mouse model, we discovered that the loss of Q-tRNA leads to learning and memory deficits. Ribo-Seq analysis in the hippocampus of *Qtrt1*-deficient mice revealed not only stalling of ribosomes on Q-decoded codons, but also a global imbalance in translation elongation speed between codons that engage in weak and strong interactions with their cognate anticodons. While Q-dependent molecular and behavioral phenotypes were identified in both sexes, female mice were affected more severely than males. Proteomics analysis confirmed deregulation of synaptogenesis and neuronal morphology. Together, our findings provide a link between tRNA modification and brain functions and reveal an unexpected role of protein synthesis in sex-dependent cognitive performance.

Keywords learning and memory; protein translation; queuosine; sex bias; tRNA modifications
Subject Categories Neuroscience; RNA Biology

Introduction

During protein synthesis, tRNA serves as a key adaptor molecule that links the transcriptome to the proteome by base pairing with cognate mRNA codons. The flexibility of codon–anticodon interactions enables many tRNAs to decode multiple codons at various levels of efficiency and stability (Lehmann & Libchaber, 2008; Grosjean & Westhof, 2016). This phenomenon is known as codon degeneracy, a form of translational regulation governed by biased codon usage and post-transcriptional modifications located at/or adjacent to the tRNA anticodon loop (Hou *et al*, 2015). While the interactions between the first codon base and the third anticodon base, as well as the second codon base and the second anticodon base, strictly adhere to canonical Watson–Crick base-pairing rules, the association between the third codon base and the first anticodon base (position 34) frequently accommodates non-canonical base pairings, collectively called "wobble pairings" (Crick, 1966). These interactions are facilitated by a large number of anticodon loop modifications, especially wobble modifications (Agris *et al*, 2017). Among all

1   Division of Epigenetics, DKFZ-ZMBH Alliance, German Cancer Research Center (DKFZ), Heidelberg, Germany
2   Faculty of Biosciences, Heidelberg University, Heidelberg, Germany
3   Department of Neurology, Medical Faculty Mannheim, Heidelberg University, Mannheim, Germany
4   Interdisciplinary Center for Neurosciences, Heidelberg University, Heidelberg, Germany
5   Université Paris Cité, Génomes, Biologie Cellulaire et Thérapeutique U944, INSERM, CNRS, Paris, France
6   Center for Molecular Biology of Heidelberg University (ZMBH), DKFZ-ZMBH Alliance, Heidelberg, Germany
7   Division of Biochemistry, Mannheim Institute for Innate Immunoscience (MI3), Mannheim Cancer Center (MCC), Medical Faculty Mannheim, Heidelberg University, Mannheim, Germany
8   Department of Infection and Immunity, Luxembourg Institute of Health, Strassen, Luxembourg
9   Division of Neurodegenerative Disorders, Department of Neurology, Medical Faculty Mannheim, Mannheim Center for Translational Neurosciences, Heidelberg University, Mannheim, Germany
10 Interdisciplinary Neurobehavioral Core (INBC), Medical Faculty Heidelberg, Heidelberg University, Heidelberg, Germany
11 Transgenic Service W450, German Cancer Research Center (DKFZ), Heidelberg, Germany
12 Department of Life Sciences and Medicine, University of Luxembourg, Luxembourg
13 Institute of Pharmaceutical and Biomedical Science (IPBS), Johannes Gutenberg-University Mainz, Mainz, Germany
14 Mannheim Center for Translational Neuroscience and Institute for Innate Immunoscience, Medical Faculty Mannheim, Heidelberg University, Mannheim, Germany
    *Corresponding author. Tel: +49-621 38371439; Fax: +49-621-38371435; E-mail: francesca.tuorto@medma.uni-heidelberg.de

identified wobble modifications, queuosine (Q), a hyper-modified guanosine analog consisting of a 7-deazaguanosine core, is one of the most complex base changes. It is present on four mitochondrial and four cytoplasmic tRNA species decoding the dual synonymous NAU/C codons: tRNA[Tyr], tRNA[His], tRNA[Asn], and tRNA[Asp] (Suzuki & Suzuki, 2014; Fergus et al, 2015, 2021).

To modify tRNAs with Q, eukaryotes exclusively rely on bacterial queuine (q) as a resource (Reyniers et al, 1981; Kirtland et al, 1988; Siard et al, 1991; Gaur et al, 2007; Tuorto et al, 2018; Muller et al, 2019). Bacterial q is acquired and salvaged by mammals from their diet, gut microbiota, and ingested food (Reyniers et al, 1981; Katze et al, 1982). After its uptake, q is inserted into specific tRNAs by the tRNA guanine transglycosylase (TGT) enzyme complex. In eukaryotes, the TGT complex comprises a catalytic subunit, QTRT1, and a homologous accessory subunit, QTRT2 (formerly known as QTRTD1) (Sebastiani et al, 2022). The eukaryotic TGT complex was found to localize on the outer mitochondrial membrane (Boland et al, 2009), where it presumably modifies both cytoplasmic and mitochondrial tRNA substrates.

Even though the majority of base exchanges are incorporated into the tRNA individually, the formation of several tRNA anticodon loop modifications is interconnected (Han & Phizicky, 2018). For instance, DNMT2-mediated methylation is stimulated by the micronutrient q (Muller et al, 2015; Tuorto et al, 2018; Nagaraja et al, 2021). Although it is uncertain how q promotes the formation of C38 methylation on tRNA[Asp]$_{GUC}$, it is anticipated that Q-tRNA modification might regulate the DNMT2 activity by participating in a mechanism that changes the enzymatic affinity of DNMT2 (Ehrenhofer-Murray, 2017).

Wobble modifications control the strength of codon–anticodon interactions, thereby influencing the efficiency of codon-biased translation of mRNA subsets. By adjusting the frequency of wobble modifications, cells are thought to canalize resources for synthesizing essential proteins, for example, during environmental stress (Duechler et al, 2016). Recently, we discovered a direct connection between Q and the speed of codon-biased translation, whereby Q-dependent translational regulation at the level of single codons, especially at Q-decoded and near cognate codons, promotes protein folding and prevents the accumulation of misfolded proteins (Tuorto et al, 2018).

To date, axenic mouse models that were fed a q-free diet (Reyniers et al, 1981; Tuorto et al, 2018), as well as a genetic Qtrt1 gene trap mouse model (Rakovich et al, 2011), have been established to explore the physiological function of Q. These models have mainly focused on the biochemical function of q and Q-tRNA modification. For example, it was reported that feeding Qtrt1 gene trap mice a tyrosine-free diet compromises the ability of mice to produce tyrosine from phenylalanine due to a decrease in the level of cofactor tetrahydrobiopterin (BH4; Rakovich et al, 2011). Aside from its established role in tyrosine synthesis, BH4 is also involved in the biosynthesis of several neurotransmitters, including dopamine (Homma et al, 2013). Given the central role of dopamine deficiency in Parkinson's disease (Ruitenberg et al, 2021), the lack of Q was proposed to result in symptoms resembling those observed in Parkinson's disease (Bednarova et al, 2017; Skolnick & Greig, 2019). Moreover, in in vitro models of Parkinson's and Alzheimer's diseases, treatment with chemically synthesized q resulted in increased neuronal survival (Richard et al, 2021).

Furthermore, the lack of Q-tRNA modification has been linked to several other neurological and neuropsychiatric diseases, such as multiple sclerosis (MS) and schizophrenia (Bednarova et al, 2017; Varghese et al, 2017). The potential medical significance of Q-tRNA modification has been shown in a mouse model for MS by reversing the clinical symptoms of MS with the administration of 6-thioguanine as a TGT substrate (Varghese et al, 2017). Although modulation of Q may have therapeutic potential based on these published studies, it should be noted that the impact of Q-tRNA modification on neuronal physiology is not entirely conclusive.

Here, we focused on the role of Q in protein translation and murine brain function by generating a mouse line lacking the catalytic subunit of the TGT complex, QTRT1. Our ribosome profiling analysis revealed that Q-tRNA modification enhances the translation speed of Q-decoded codons in the murine hippocampus, and thereby increases the overall speed of rapidly translated codons. In agreement with the behavioral phenotype, the effect on protein synthesis was more pronounced in female mice, emphasizing the critical function of Q in the neuronal architecture of the hippocampus and ultimately, in the sex-dependent learning and memory abilities.
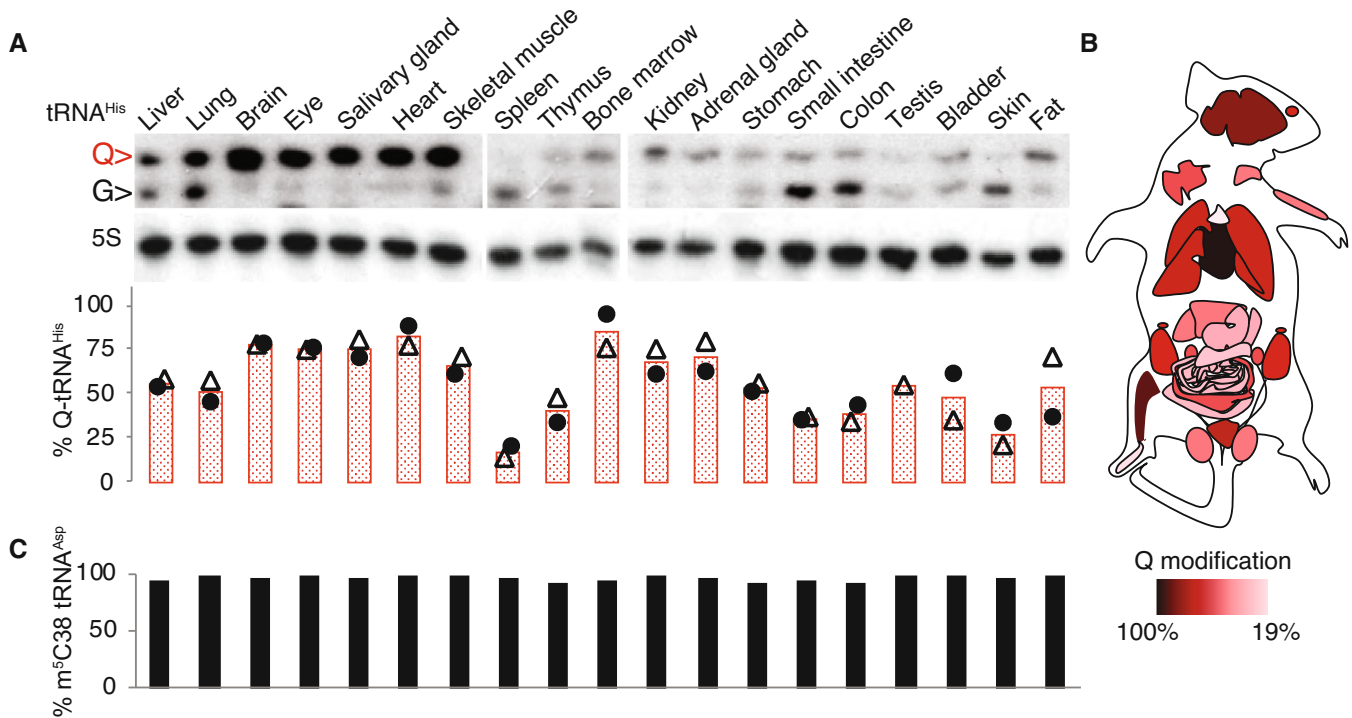
Results

Q-tRNA levels vary between murine tissues

An increasing number of studies has revealed that the extent of Q differs between tissues, metabolic states, and developmental stages (Singhal et al, 1981; Nishimura, 1983; Costa et al, 2004; Zaborske et al, 2014; Thumbs et al, 2020). While these reports provide Q-tRNA modification patterns in several tissues and organisms, a comprehensive analysis is so far lacking.

Q modification can be measured in an individual tRNA by comparing the migration of modified and unmodified tRNAs in a polyacrylamide gel that is covalently linked to N-acryloyl-3-aminophenylboronic acid (APB), followed by Northern blot analysis (Igloi & Kossel, 1985; Cirzi & Tuorto, 2021). We, therefore, analyzed the tissue-specific distribution of Q-tRNA modification in tRNA[His] and tRNA[Asn] in up to 20 adult murine tissues using APB Northern blotting (Fig 1A and Appendix Fig S1A and B). Additionally, the tissue-specific distribution of Q modification was confirmed by measuring the Q content relative to G in total RNA using LC–MS/MS (Fig 1B and Appendix Fig S1C). Both APB Northern blot and LC–MS/MS results showed that Q modification is ubiquitously present in all tissues, with brain, heart, and skeletal muscle having higher Q levels. This distribution was reflected only partially by the expression level of Qtrt1 (Appendix Fig S1B, C and D), which is consistent with the notion that other factors, for example, tissue turnover rate, are important to determine the level of Q modification.

Among all Q-modified tRNAs, tRNA[Asp] is the only tRNA species modified with both Q at position 34 and m[5]C at position 38. Previously, we demonstrated that DNMT2-mediated tRNA[Asp] methylation is enhanced by queuosinylation in human cells and several murine tissues (Tuorto et al, 2018). To determine whether the crosstalk between DNMT2-mediated tRNA methylation and Q occurs in a wider range of murine tissues, we performed targeted tRNA[Asp] bisulfite sequencing. High levels (~ 96%) of m[5]C38 in tRNA[Asp]$_{GUC}$ were observed in all tissues (Fig 1C), including in spleen and skin,

Figure 1. Q modification atlas.

A Representative APB Northern blot analysis showing differences in the levels of Q-tRNA^His modification between 19 tissues isolated from a 3-month-old female (dot) and male (triangle) mouse; bars represent the mean. 5S rRNA is shown as a loading control. The percentage of Q-tRNA was obtained by dividing the Q signal by the overall signal of Q and G. Data are represented as mean; ($n = 2$).

B Scheme of tissue-specific Q modification pattern in total RNA based on LC–MS/MS measurements. The highest Q modification containing tissue and heart was considered as 100%. The color scale indicates the relative level of Q modification in total RNA.

C C38 methylation of tRNA^Asp_GUC (m^5C38) was measured by amplicon-based RNA bisulfite sequencing on the same tissue of (A).

Data information: Q, Queuosine-tRNA; G, Guanosine-tRNA.
Source data are available online for this figure.

which have relatively low levels of Q ($\sim 20\%$). Hence, the physiological level of Q is sufficient for complete C38 methylation on tRNA^Asp_GUC in murine tissues.

The loss of Q-tRNA modification impairs cognitive functions

To establish a mouse model that is entirely free of Q-tRNAs, we disrupted the *Qtrt1* gene. Using CRISPR/Cas9-mediated genome editing in E14 mouse embryonic stem cells (mESCs) (Appendix Fig S2A and B), we induced a wide range of insertion–deletion (indel) events in the third exon of the *Qtrt1* gene. These frameshift mutations ranged from single-nucleotide to 19-nucleotide indels, located 0–4 bp upstream of the proto adjacent motif sequence (NGG). The mutant mouse line (Q1; C57BL/6J-*Qtrt1*^em1Tuo) was generated using mESCs carrying an additional thymine (T) on one allele of the third exon (Fig 2A). To eliminate potential off-target mutations, the mutant mice were crossed for six generations into a C57BL/6J background. Western blot analysis confirmed the absence of QTRT1 protein expression in the mutant mice (Fig 2B). Importantly, APB-Northern blotting and LC–MS/MS analysis revealed the absence of Q-modified tRNAs in the *Qtrt1*-deficient mice (Fig 2C and D), validating the successful generation of a non-functional *Qtrt1*

allele. Finally, we analyzed the crosstalk between DNMT2-mediated C38 methylation of tRNA^Asp_GUC and Q using amplicon-based bisulfite sequencing. The results indicated that C38 methylation is reduced up to 40% in the adult Q1 hippocampus (Fig 2E), confirming the dependency of C38 methylation on Q-tRNA modification.

The Q1 mice were viable and fertile without any obvious changes in their overall development or growth (Appendix Fig S3). Also, no sex bias within the progeny was observed. Interestingly, during backcrossing, Q1 mice developed an excessive self-grooming behavior. Therefore, in the final C57BL/6J background, Q1 adult mice were subjected to a comprehensive battery of behavioral tests (Appendix Table S1), with a focus on learning and memory functions of the hippocampus.

We analyzed mice of both sexes and compared mutant mice with corresponding control of the same sex (Figs 3–7). First, we performed open-field and home-cage (LABORAS) observation tests to examine locomotor activity and anxiety-like behavior in either a novel or in a known environment. We found that Q1 female mice traveled less distance in the center of the Open-field chamber than wild-type female mice, while the total travel distance in the chamber did not differ between genotypes (Fig EV1A–C). Nevertheless, LABORAS, a system that allows unbiased observations of
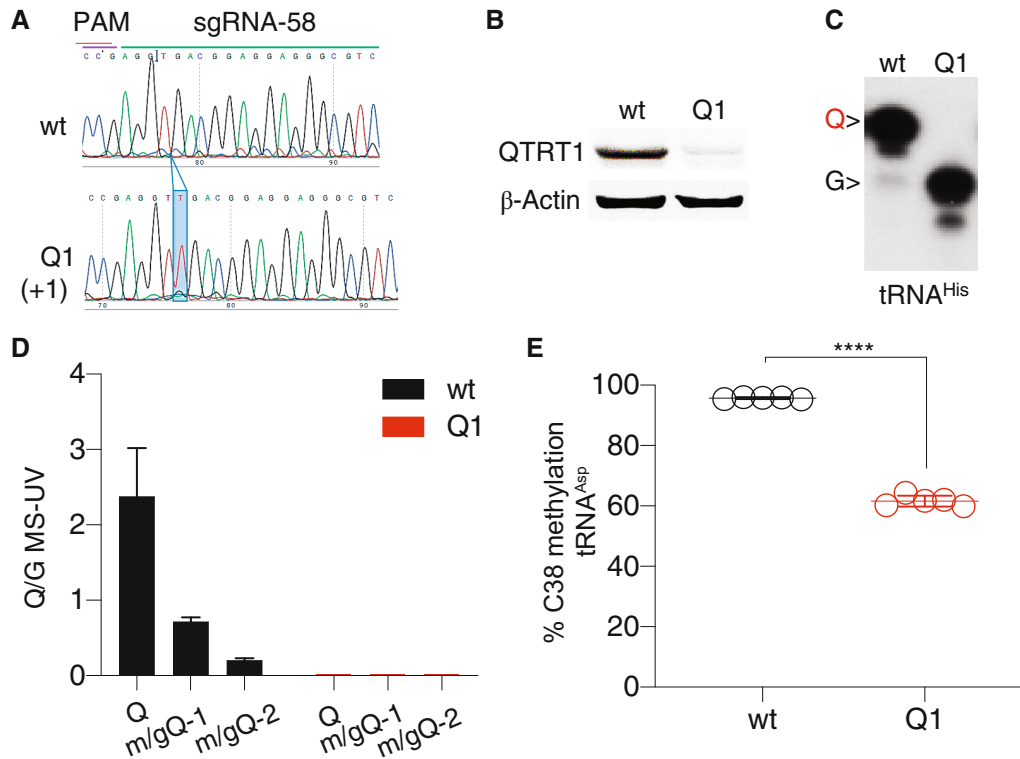
Figure 2. Generation of a *Qtrt1*-deficient mouse line using CRISPR/Cas9 technology.

Qtrt1 knockout mouse model (Q1) was verified at genomic, protein, and functional levels.

A   PCR amplicon-based sequencing chromatogram covering the mutated (Q1) site shows the insertion of a T nucleotide in the third exon of the *Qtrt1* gene. The chromatograms are shown in the 5′–3′ orientation. (+1) Indicates insertion of one nucleotide, T. PAM: proto adjacent motif.

B   The mutation causes loss of QTRT1 protein. 100 μg of total protein isolated from a 7-month-old hippocampus was analyzed by Western blotting using anti-QTRT1 antibody. β-Actin was used as a loading control.

C   Insertion of T nucleotide in the *Qtrt1* gene results in complete loss of Q-tRNA^{His} modification in the Q1 brain. 5 μg of RNA was separated on an APB gel and hybridized with tRNA^{His} oligonucleotide probe.

D   Mass spectrometry quantification of Q, galactosyl-Q or mannosyl-Q levels in total RNA isolated from the brain tissue. Data are represented as mean ± SD; ($n = 3$ technical replicates).

E   Reduced DNMT2-dependent methylation levels were determined by RNA bisulfite sequencing in the Q1 hippocampus. Each dot represents an individual. Error bars represent ±SD; ($n = 5$). ****P-value < 0.0001, two-tailed unpaired t-test.

Data information: G, Guanosine-tRNA; gQ, Galactosyl-Q; mQ, Mannosyl-Q; Q, Queuosine-tRNA; Q1, *Qtrt1* knockout mouse; wt, wild-type mouse.
Source data are available online for this figure.

spontaneous behavior, revealed a significant increase in activities related to speed and locomotion in the Q1 female mice (Fig EV1D–F and Appendix Fig S4). These differences between genotypes were not observed when comparing Q1 mutant males with respective wild-type mice (Fig EV1D–F). The open-field and LABORAS tests provided first hints that the loss of Q in female mice induced anxiety-like and hyperactivity behavior. Nevertheless, dark/light box test excluded major defects in exploration functions and anxiety, and rotarod and grip strength tests excluded significant deficiencies in motor behavioral functions (Appendix Fig S5).

Next, we used three behavior methods on two cohorts of mice (I. cohort $n = 6$, II. cohort $n \geq 8$) to assess hippocampal-dependent learning and memory functions by Morris water maze (MWM), IntelliCage, and Fear conditioning. With the first cohort of mice, MWM (Appendix Fig S6) was used to assess spatial learning and memory. Before the MWM trials, mice were trained with a visible platform to exclude differences between groups in

navigation skills (Fig EV1G). During trials with the hidden platform, both learning (Fig EV1H and I) and success rate (Fig EV1J) were decreased in Q1 female mice that showed also a notable reduction in the time spent in the quadrant containing the former platform in the probe trial on day 12 (Fig EV1K–M). However, male mice, both wt and Q1, were in general less performant, which renders the evaluation of their learning capacity difficult (Fig EV1I–M).

Thus, we subsequently monitored spatial learning and memory in the second cohort of mice using IntelliCage (Kiryk *et al*, 2020; New Behavior, Zurich, Switzerland), a system for unbiased monitoring of mouse behavior in a home cage setting (Appendix Fig S7). The female Q1 mice were confirmed to be hyperactive as demonstrated by the high number of visits registered in the four corners of the cage (Fig 3A). In addition, hippocampal-dependent place learning and reversal place learning were significantly impaired in Q1 female mice as indicated by the increased error percentage in the

correct drinking place (Fig 3B and C) and corresponding reduction in correct corner visits with nose poke and drinking (Fig 3D).

Lastly, all the mice were tested for formation and retrieval of hippocampal memory using another well-known paradigm, fear conditioning (Appendix Fig S8). Again, Q1 female mice showed significantly less conditioning, context, and cue-related freezing behaviors and impaired

context-dependent learning and memory, while male Q1 mice were as responsive as their wild-type littermates (Fig 3E).

Taken together, behavior tests revealed that female Q1 mice are hyperactive and that learning and memory are impaired in the adult Q1 mice, with Q1 females being more affected than Q1 male mice when compared to relative wild-type counterparts.
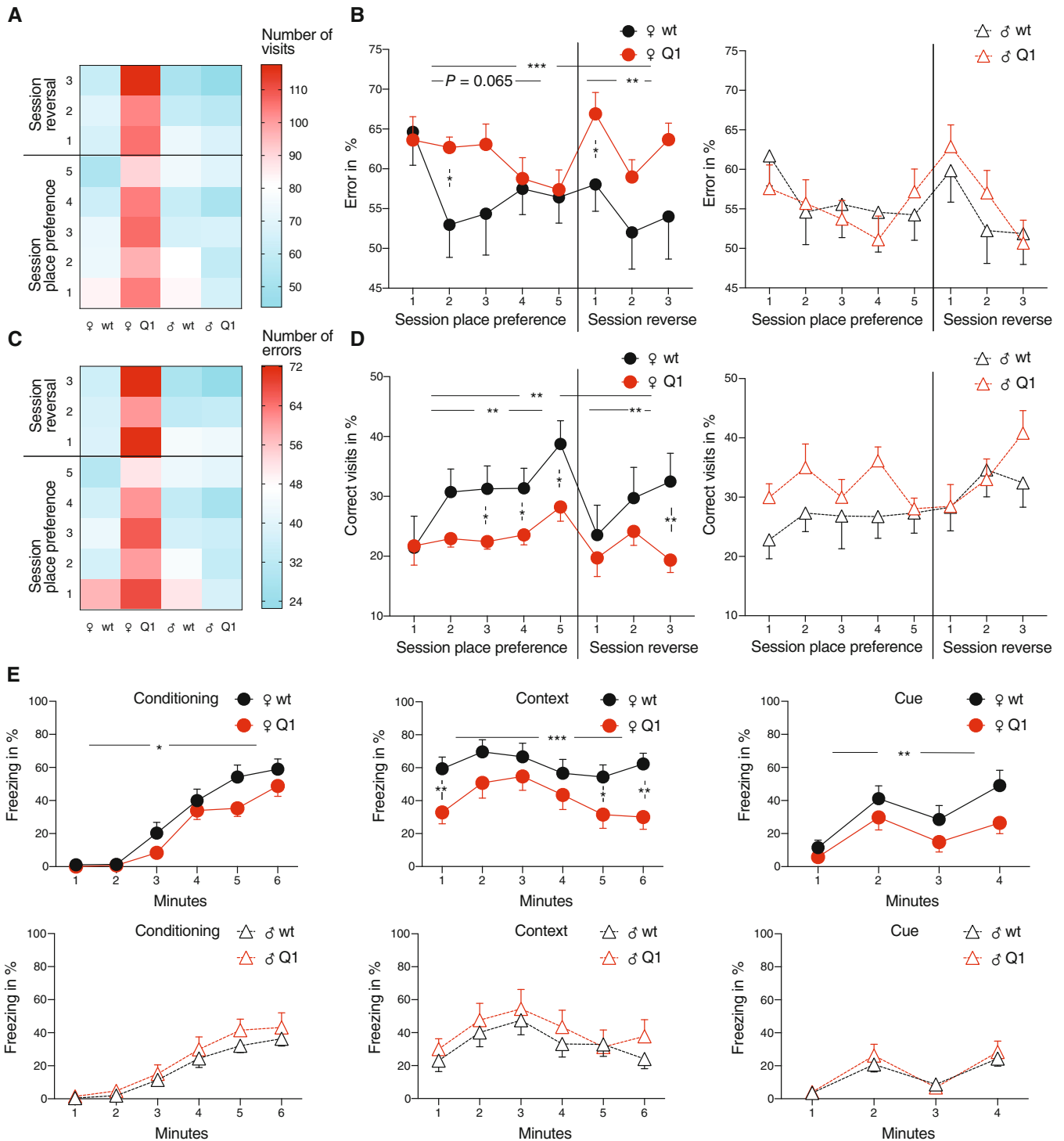

Figure 3.

Figure 3. The loss of Q hampers learning and memory formation.

A Mice were tested for place learning and reversal place learning using IntelliCage. During the 5 days of place learning sessions, each animal has free access to water at only one specific corner in the cage and visits to any other corner are registered as an "error". During the 3 days of place reversal sessions, the water access corner is switched to the diagonally opposing site. Heatmap showing the medium number of visits for each animal group during the place preference and reversal sessions in the IntelliCage test.

B Percentage of erroneous visits in the max activity time (first 8 h of the night) for each session is presented as a measure of learning performance. Error bars are represented as ±SEM. Statistical significance was analyzed by beta regression. Effect of sex on overall genotypes has *P*-value = 0.01827. Significant *P*-values for genotype effect (Q1 versus wt) for the entire session and at time points are indicated.

C Heatmap showing the number of erroneous visits for each animal group during the place preference and reversal sessions.

D Percentage of the number of visits to the correct corner with nose poke and a minimum of one lick in the same session period of (C). Error bars are represented as ±SEM. Statistical significance was analyzed by beta regression. Effect of sex on overall genotypes has *P*-value = 0.0000249. Significant *P*-values for genotype effect (Q1 versus wt) for the entire session and at time points are indicated. For (A) to (D) Female *n* = 8 wt and *n* = 10 Q1; male *n* = 8 wt and *n* = 8 Q1.

E wt and Q1 mice were subjected to fear-conditioning test. Percentage of freezing behavior is shown minute by minute during conditioning, contextual, and cued tests. Error bars are represented as ±SEM. Statistical significance was analyzed by beta regression. Effect of sex on overall genotypes has *P*-value = 0.06461 for conditioning, *P*-value = 0.001254 for contextual, and *P*-value = 0.0951 for cued tests. Significant *P*-value for genotype effect (Q1 versus wt) for the entire session and at discrete time points are indicated in the graphs. Female *n* = 14 wt and *n* = 16 Q1; male *n* = 14 wt and *n* = 14 Q1.

Data information: Q1, *Qtrt1* knockout mouse; wt, wild-type mouse. *P-value < 0.05, **P-value < 0.01; ***P-value < 0.001.
Source data are available online for this figure.

The absence of Q-tRNA modification alters hippocampal plasticity

To understand whether the observed behavioral phenotypes were associated with alterations of brain morphology or alterations in cellular compositions, we initially examined gross brain morphology, the organization of cell layers within major regions, brain weight, and a number of brain-resident glial cells, astrocytes, oligodendrocytes, and microglia in the Q1 hippocampi. These analyses revealed no major changes between the genotypes (Fig EV2A–D). Also, we did not detect any increased cell death in the Q1 hippocampi, monitored by TUNEL assay (Fig EV2E), at the tested age.

Changes in neuronal composition of the hippocampus were investigated using an mRNA *in situ* hybridization assay for the neuronal marker gene, synaptotagmin 1 (*Syt1*; Fig 4A). SYT1 is an integral membrane protein of synaptic vesicles that triggers neurotransmitter release at the synapses of post-mitotic neurons (Fernandez-Chacon *et al*, 2001). Here, we observed a consistent, approximately two fold, reduction in the number of *Syt1*-expressing cells in the Q1 hippocampus, particularly in the dentate gyrus (DG), a part of hippocampal formation that is directly implicated in learning and memory formation (Hainmueller & Bartos, 2020) and CA1 region that is also important for memory formation and spatial navigation (Benavides-Piccione *et al*, 2020; Fig 4A and B). On the other hand, our RNA-seq analysis revealed no change in the overall expression of *Syt1* mRNA in the Q1 hippocampus when compared to wild-type littermates (Dataset EV1), suggesting that the loss of Q results in decreased neuronal density in the analyzed hippocampal regions. However, since we cannot exclude a local decrease in *Syt1* mRNA expression, we performed immunohistochemical assays using a neuronal nuclei marker (NeuN) (Gusel'nikova & Korzhevskiy, 2015; Fig EV3A). By this approach, we confirmed decreased neuronal density in the DG of the Q1 mice and a non-statistically significant trend in the CA1 region (Fig 4C and D). Therefore, both Q1 sexes are affected in their hippocampal neuronal density, however, again the deficits are more pronounced in the Q1 females in comparison to their wild-type counterparts, than in the Q1 males.

Next, we performed Golgi-Cox staining to assess potential alteration of the neural architecture in the dentate gyrus (Fig EV3B). Our results showed that the total dendritic length of granular pyramidal neurons is significantly reduced in the dentate gyrus of female Q1 mice (Fig 4E) and arborization is significantly altered in both sexes (Fig 4F). Nevertheless, the density and morphology of dendritic spines remained similar between wild-type and Q1 animals (Fig EV3C–E).

Taken together, these findings suggest that structural alteration of hippocampal pyramidal neurons in the Q1 mice results in a reduced cell density, which potentially contributes to sex-dependent defects in learning and memory formation of the Q1 female mice.

Figure 4. Neuronal composition is altered in the Q1 hippocampus.

A Representative *Syt1* staining in the 7- to 8-month-old female mice. *Syt1* mRNA expression colocalizes with nuclei of post-mitotic neurons. Red: *Syt1* mRNA, blue: DAPI. Scale bar 500 μm.

B The number of *Syt1*+ cells was counted in the dentate gyrus (DG) and CA1 using ImageJ. Error bars represent ±SD (*n* ≥ 3). Statistical significance was analyzed by two-tailed unpaired *t*-test.

C Representative images of IHC staining for NeuN in the DG of 8-month-old female mice. Scale bar 250 μm.

D Quantification of NeuN+ cells in the DG and CA1 using ImageJ. Error bars represent ±SD; (*n* = 5). Statistical significance was analyzed by two-tailed unpaired *t*-test.

E Representative images and dendrite lengths of Golgi-Cox-stained pyramidal neurons in the DG area of 8-month-old female wild-type and Q1 mice. Red asterisks indicate pyramidal neurons with short dendrites in the Q1 mice. Scale bar: 10 μm. Error bars represent ±SD; (*n* = 5; 20 dendrites per replicate). Statistical significance was analyzed by two-tailed unpaired *t*-test.

F Sholl analysis of the complexity of neuronal dendritic arbors in the DG. Error bars represent ±SEM; (*n* = 15; 3 neurons per animal and 5 animals per genotype/sex).

Data information: DG, dentate gyrus; Q1, *Qtrt1* knockout mouse; wt, wild-type mouse. *P-value < 0.05, **P-value < 0.01, ***P-value < 0.001.
Source data are available online for this figure.

Figure 4.
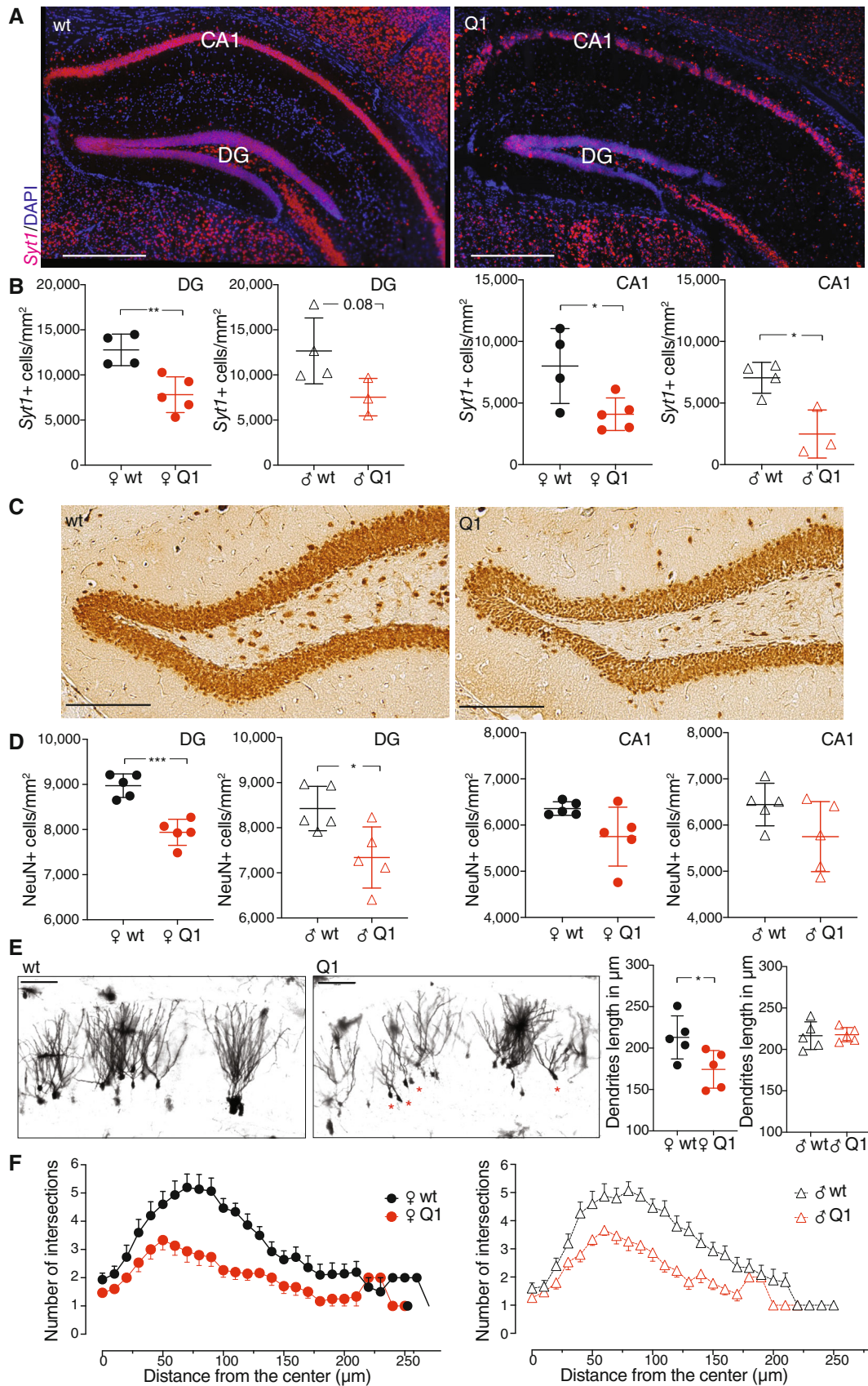
The absence of Q-tRNA modification leads to a global imbalance in the speed of codon-biased translation

To explore the molecular mechanism underlying the behavioral and histological deficits in the Q1 mice, we examined protein translation in the hippocampus of adult mice. First of all, to exclude any major effect of tRNA availability on translation, we measured the levels of selected Q-tRNA species and found no difference between wild-type and Q1 hippocampi (Fig EV4A). Also, polysome profiling analysis showed that the overall translation rate is similar between wild-type and Q1 hippocampi (Fig EV4B).

Nevertheless, given that Q-tRNA modification is involved in translation of specific codons (Tuorto *et al*, 2018), we next carried out ribosome profiling (Ribo-Seq, (Ingolia *et al*, 2009)), which allowed to assess mRNA-specific translation at single codon resolution (Dataset EV1). To evaluate the quality of our ribosome profiling data, the coverage of Ribo-Seq reads across coding regions and periodicity of the 5′ ends of Ribo-Seq reads were determined using the RiboVIEW pipeline (Legrand & Tuorto, 2020), demonstrating the high quality of our datasets (Fig EV4C and D). In total, ribosomal footprints could be mapped to > 7,700 mRNAs in the hippocampi of each genotype (Fig EV4E). Codon enrichment (CE) analysis (Legrand & Tuorto, 2020) revealed that specific codons are enriched or depleted in the Ribo-Seq reads upon the loss of Q-tRNA modification and reduced C38 methylation of tRNA$^{Asp}_{GUC}$ (Fig 5A), suggesting slow or fast translation, respectively, at these codons. In line with our previous observations (Tuorto *et al*, 2018), the enriched codons included the Q-decoded codons AAU and AAC (tRNA^{Asn}), GAU and GAC (tRNA^{Asp}), and CAU (tRNA^{His}). By comparing the synonymous codon pairs, we found that U-ending codons were slowed down more severely than C-ending codons, except for UAU (tRNA^{Tyr}), which appeared to be unaffected by the loss of Q (Fig 5A).

Strikingly, Q-tRNA ablation did not only affect Q-decoded codons but led to a general, statistically significant enrichment of footprints carrying A/U-rich codons in the A-site, codons in which at least two bases are either an A and/or U (Fig 5A and B). This translational slowdown was especially prominent on Phe and Leu codons that start with U and contain at least one additional U in the codon triplet. On the other hand, G/C-rich codons were translated more rapidly in the absence of Q-tRNA modification (Fig 5A and B). This imbalance is possibly linked to the translation kinetics of strong and weak codon–anticodon interactions based on the structure and energy classification of codon–anticodon pairings (Grosjean & Westhof, 2016). According to this classification, codons containing A and/or U in the first two positions are considered weak, whereas codons with C and/or G in the first two positions are considered strong (Grosjean & Westhof, 2016). In our Ribo-Seq analysis, we observed a significant enrichment of footprints with weak A-site codons upon loss of Q-tRNA modification (Fig 5A and C). This may be similar to a "traffic jam" situation, whereby the reduction in local translation speed at Q-decoded codons causes the slowdown of all the rapidly translated (i.e., weak) codons. In agreement with this model, we observed an increased footprint coverage on codons preceding Q-decoded codons, but not on codons following Q-decoded codons, specifically in the hippocampi of female Q1 mice (Fig 5D). Consistent with the CE analysis (Fig 5A and B), the "traffic jam" was more pronounced for A/U-rich codons (Fig 5D). While A/U-rich codons were slowed down in both female and male hippocampi, female mice were found to be more severely affected (Fig 5B–D), which is consistent with the female bias in the behavior and histological analyses (Figs 3 and 4). To test whether the sex-dependent phenotype observed in this study is dependent on the extent of Q, we analyzed the Q-tRNA modification level in the hippocampus of female and male mice, and yet could not observe any significant difference between sexes (Fig EV4F).

To characterize the effect of Q on the translation of individual mRNAs, we calculated the ribosome density (RD), defined as the ratio between ribosomal footprints and mRNA expression level, for every expressed gene. Among >10.000 mRNAs for which RDs could be calculated (Dataset EV1), 327 differentially translated genes were detected in the female Q1 hippocampi, but only 92 in male Q1 (Fig 6A), with 38 transcripts overlapping between male and female (Fig EV4G) and confirming once again the sex-dependent effect of Q ablation.

Since the loss of Q differentially changes translation speed at A/U- and G/C-rich codons, we wondered if this imbalance could alter the translation rate of G/C-rich ORFs. We, therefore, plotted the GC

Figure 5. Q-tRNA modification regulates codon-biased translation in the adult hippocampus.

A   Changes in bulk codon enrichment (CE) at ribosome A site in the 6- to 7-month-old Q1 hippocampi compared to wild-type. The overall composition of codons is highlighted in the indicated colors. A/U- or G/C-rich indicates that a codon contains at least two A and/or U or G and/or C bases, respectively. Error bars represent ±SE; (n = 5).

B   Boxplots depict the difference in codon enrichment (CE) between G/C-rich codons versus A/U-rich codons at the ribosome A site. Boxplots display the median as central band, and first and third quartiles as box limits; whiskers correspond to the box limits ± 0.75 interquartile range. The sample size is n = 32 for G/C-rich codons and n = 29 for A/U-rich codons. Replicates correspond to CE for different codon identities. CE of each codon is averaged over three biological replicates for female and two for male mice. Wilcoxon rank-sum test ***P-value < 0.001.

C   Quantification of CE of strong and weak codons at the ribosome A site. The codons were classified according to Turner energies of the codon/anticodon pairs (Grosjean & Westhof, 2016). The strong group (average − 3.1 kcal/mole): Ala (GCU, GCC, GCA, GCG), Arg (CGU, CGC, CGA, CGG), Gly (GGU, GGC, GGA, GGG), and Pro (CCU, CCC, CCA, CCG). The weak group (average − 1.0 kcal/mole): Asn (AAU, AAC), Ile (AUU, AUC, AUA), Leu (UUA, UUG), Lys (AAA, AAG), Met (AUG), Phe (UUU, UUC), and Tyr (UAU, UAC). Boxplots display the median as central band, and first and third quartiles as box limits; whiskers correspond to the box limits ± 0.75 interquartile range. The sample size is n = 16 for strong codons, and n = 14 for weak codons. Replicates correspond to CE for different codon identities. CE is averaged over three biological replicates for female and two for male mice. Wilcoxon rank-sum test ***P-value < 0.001.

D   Metagene plot of footprint coverage in the ribosome queue of Q-decoded codons. The coverage of A/U- or G/C- rich codons at each position is normalized to their respective coverage at the A site. The plots show the raw mean, the smoothed mean, and the confidence band corresponding to ±SEM (female n = 3, male n = 2).

Data information: CE, codon enrichment; Q1, *Qtrt1* knockout mouse; wt, wild-type mouse.
Source data are available online for this figure.
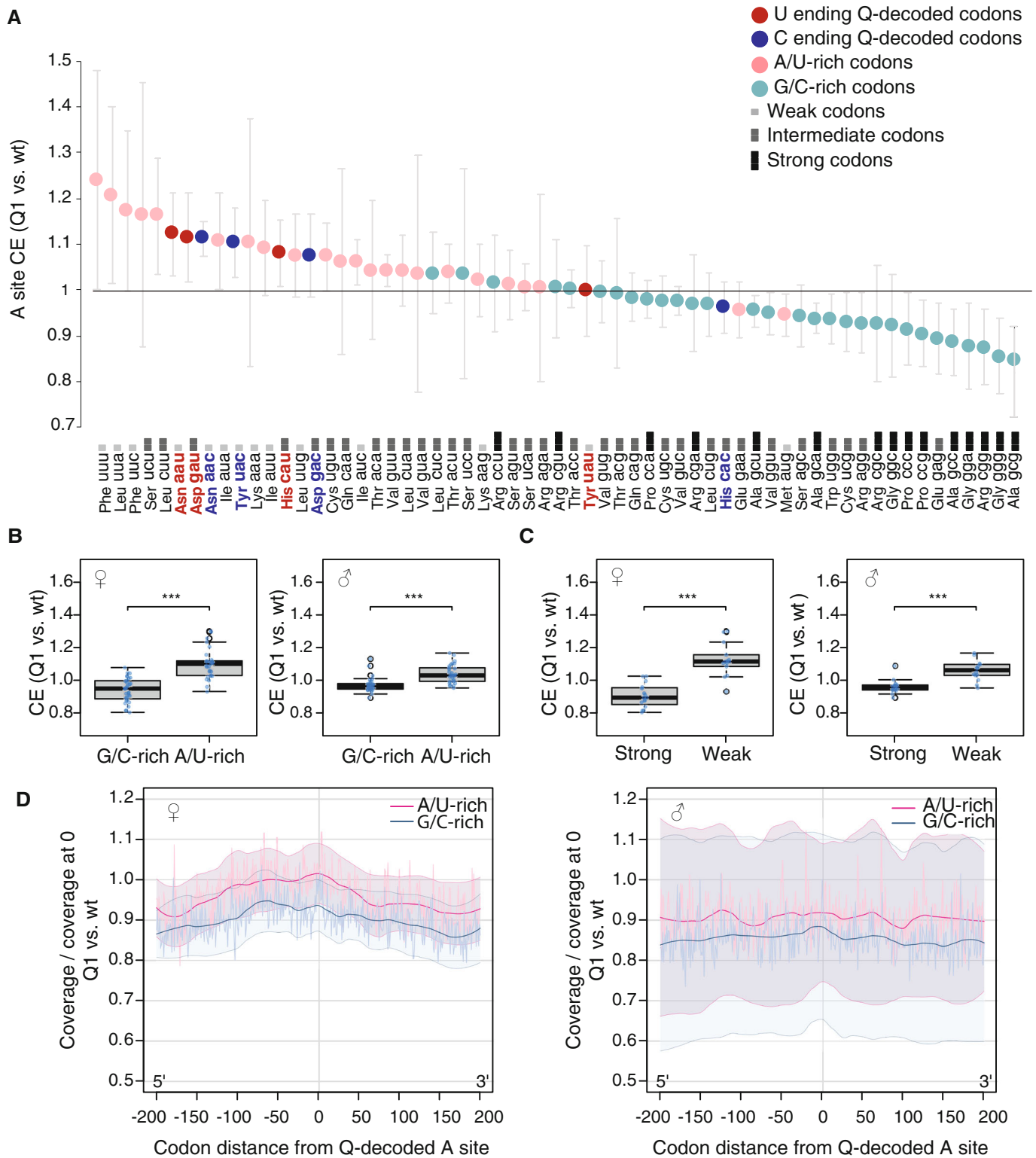
Figure 5.

content of ORFs against the change in RD between wild-type and Q1 hippocampi and found a negative, however, weak, correlation between the two parameters (Fig 6B). This suggested that ORFs with a high abundance of strong G/C-rich codons are translated more

efficiently in the Q1 hippocampi. Once again, the results were much stronger in female than male mice (Fig 6B), validating the codon enrichment data with an orthogonal approach. Our results reveal that the absence of Q-tRNA modification leads to an overall
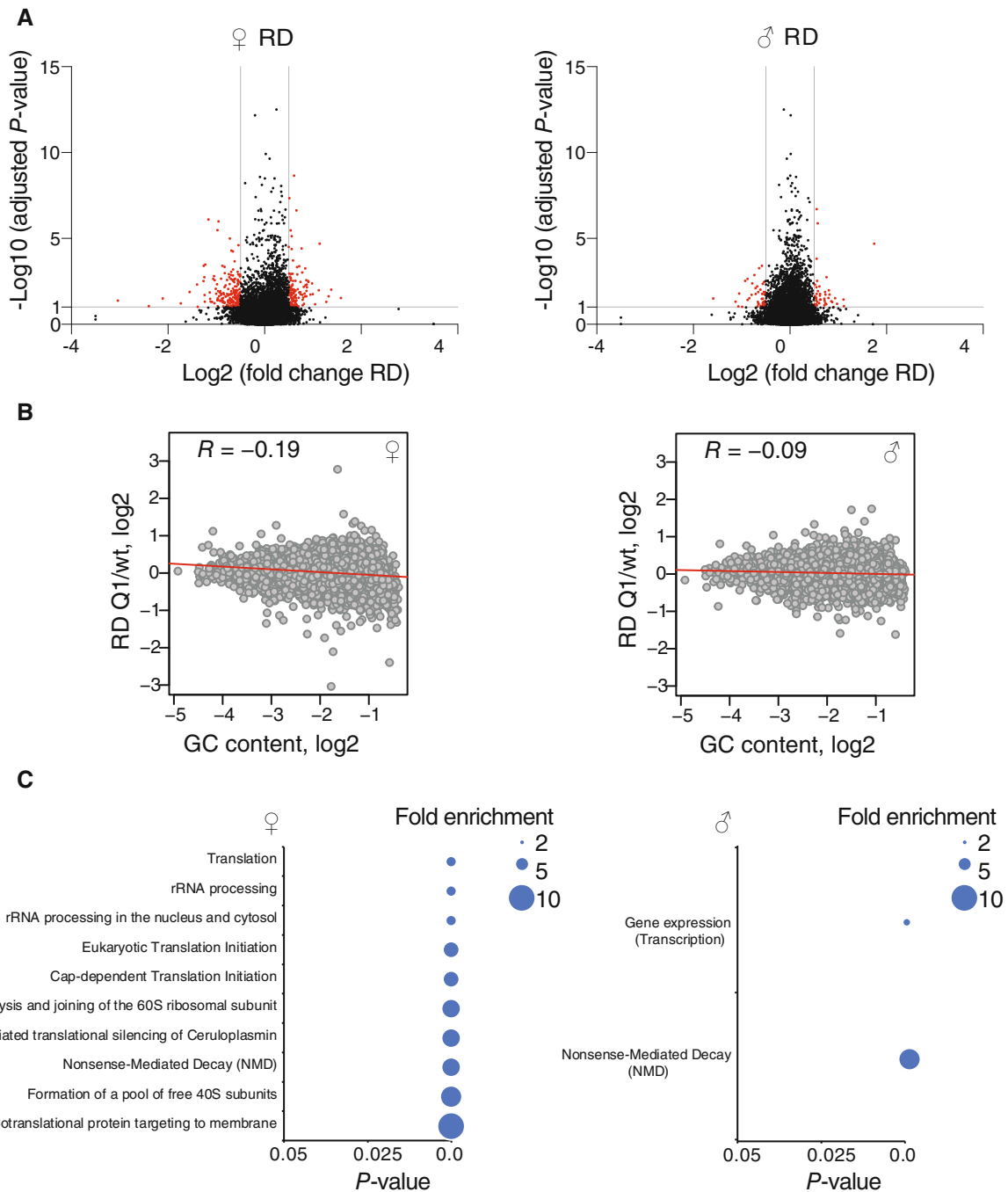
Figure 6. Ribosome density analysis in the adult hippocampus reveals sex- and genotype-dependent differences.

A   Volcano plots showing ribosome density (RD) of 6- to 7-month-old Q1 and wild-type hippocampi ($n = 5$, 2 male and 3 female). Red dots represent differentially translated genes defined as at least one fold change ($0.5 \leq \log2(FC) \leq -0.5$) and adjusted P-value < 0.1.

B   Relationship between GC content and the RD. Pearson's correlation coefficient (R) and linear regression line (red) are indicated (male $n = 2$ and female $n = 3$).

C   PANTHER reactome overrepresentation test of differentially translated genes in male and female Q1 hippocampi identifies the canonical pathways ($0.5 \leq \log2$ (FC) ≤ -0.5 and adjusted P-value < 0.1). The top 10 pathways are shown. P-value by Fischer's exact test followed by false discovery rate correction (FDR < 0.05).

Data information: Q1, *Qtrt1* knockout mouse; RD, ribosome density; wt, wild-type mouse.
Source data are available online for this figure.

imbalance in the translation speed of weak and strong codon–anticodon pairs in the murine hippocampus, beyond its immediate requirement for efficient decoding of Q-decoded codons. All

translational changes were more pronounced in females, consistent with the stronger phenotypes observed in the female Q1 mice in learning and memory functions.

The loss of Q-tRNA modification alters the hippocampal proteome

To understand the effects of altered translation speed on the translatome of Q1 hippocampi (Fig 6A), we performed gene ontology analysis and identified the most affected pathways. PANTHER reactome analysis (Mi *et al*, 2021) revealed that genes translated differentially between wild-type and Q1 hippocampi are enriched for functions in protein translation, ribosomal metabolism, and non-sense-mediated mRNA decay (NMD), especially in females (Fig 6C). This suggests that the imbalance in the translation speed due to the lack of Q causes profound perturbations in the synthesis and regulation of the translation machinery as suggested by the increased ubiquitination of ribosomal proteins RPS10 and RPS20 observed in the Q1 mice hippocampi, indicating the involvement of the ribosome quality control (RQC) pathway (Fig EV5A).

In agreement with our previous observations in HeLa cells (Tuorto *et al*, 2018), eIF2, a target of a number of kinases during stress signaling response and ribosome slowing or stalling (Ishimura *et al*, 2016), was deregulated in the Q1 hippocampi, as well as in other tissues of Q1 mice, as shown by increased eIF2α phosphorylation (Figs 7A and EV5B), again with the female being more affected than the male mice.

Finally, we took a quantitative proteomics approach and used stable isotope dimethyl-labelling (DML)-based mass spectrometry (Boersema *et al*, 2009) to resolve the proteome of Q1 hippocampi. In total, we identified 188 (12%) significantly dysregulated proteins among a total number of 1,649 quantified proteins in the female dataset and 243 (12%) dysregulated proteins among a total number of 1959 quantified proteins in the male dataset (Fig 7B and Dataset EV2). While 143 proteins (76%) showed reduced and 45 (24%) exhibited increased expression in the female dataset, 174 (71%) were reduced and 69 (29%) were increased in the male dataset. Therefore, regardless of sex, the majority of dysregulated proteins showed reduced expression in the Q1 hippocampi compared to wild-type, consistent with a protein translation defect. Gene ontology analysis of the dysregulated proteins revealed a strong enrichment for genes involved in pathways that are closely related to the observed phenotypes and essential for neuronal functions, such as myelinization in females and synaptic functions in both sexes (Fig 7C), as well as molecular functions directly connected to dysregulated protein synthesis (Fig EV5C). All in all, the quantitative proteomics analysis revealed dysregulation of several neural functions, including synaptic pathways, upon loss of Q-tRNA modification, which has significant implications in understanding the learning and memory phenotype.

Discussion

Translation elongation is governed by numerous factors, including tRNA availability, codon-anticodon binding affinity, and the interactions between the ribosome and the codon-anticodon complex (Ogle *et al*, 2003; Manickam *et al*, 2016; Brule & Grayhack, 2017). tRNA anticodon loop modifications are important determinants for codon–anticodon pairings, especially for wobble base pairing of specific tRNAs with different codons. Here, we found that the loss of Q-tRNA modification and reduced C38 methylation of tRNA$^{Asp}_{GUC}$ not

only change the translational speed of Q-decoded codons but also result in an imbalance in the translation speed of most other codons according to their base-pairing strength with the corresponding anticodons. This translational stress causes alterations in hippocampal cellular architecture, hampering learning and memory formation in a sex-dependent manner.

Sex bias exists in diverse aspects of life. Women and men, for example, have different eating habits (Li *et al*, 2012; Conti *et al*, 2020), which may alter the composition of the gut microbiota in a sex-specific manner (Bolnick *et al*, 2014). Changes in microbial diversity have been linked to the routine social activities and social deviations of mice (Wu *et al*, 2021b), as well as to a variety of disorders, including Alzheimer's disease, anxiety, autism, Parkinson's disease, and schizophrenia (Cryan *et al*, 2019; Cowan & Cryan, 2021). Although poorly understood, sex discrepancy is a known phenomenon in many of these disorders. While women are more likely to suffer from Alzheimer's disease and have more severe symptoms, men have been found to be affected by schizophrenia at higher frequencies (Jackson *et al*, 2013; Mendrek & Mancini-Marie, 2016; Snyder *et al*, 2016). Susceptibility to various other neurological disorders has also been found to differ between male and female individuals, including a 4:1 ratio in autism spectrum disorders (Werling, 2016) and a 1:2 ratio in depression (Kang *et al*, 2020), respectively. Also, female-to-male sex ratio of multiple sclerosis has been increasing over the last years (Orton *et al*, 2006). On the other hand, sex differences in frequency and symptoms of other neurological disorders like attention deficit hyperactivity disorder (ADHD), one of the most prevalent childhood disorders today, are still debated because most previous studies included a limited proportion of girls and relied on subjective measures of ADHD prone to bias, opening the question of a correct diagnosis of affected girls (Slobodin & Davidovitch, 2019). While the impact of the microbiota on these disorders remains to be understood (Cryan *et al*, 2019), microbial diversity may lead to differences in the salvage of bacterial q and thereby contribute to the sex bias in these neurodegenerative and mental disorders.

To understand why the learning and memory phenotype in the Q1 mice is sex-dependent, we examined possible interconnections between Q and sex. However, neither tRNA availability nor the level of Q-tRNA modification in the hippocampus was different between female and male mice (Fig EV4A and F). Thus, the sex bias in the phenotype of the Q1 mice appears to be more indirect, for example, through a higher susceptibility of females to certain neurological disorders. In fact, it should be noted that wild-type female mice outperformed males in all the behavioral tests (Figs 3 and EV1) as observed previously (Papaleo *et al*, 2012; Tucker *et al*, 2016), and that the loss of Q-tRNA canceled out the advantage of female mice. This opens the question if the higher performance of female mice in learning and memory tests is linked to a difference in protein translation.

Many studies have shown that Q levels differ between tissues and developmental stages (Nishimura, 1983; Beier *et al*, 1984; Zaborske *et al*, 2014; Thumbs *et al*, 2020). Yet, an in-depth analysis of tissue-dependent Q-tRNA modification has so far been lacking, hindering progress in understanding the role of Q in higher organisms. Here, we present an atlas for the murine tissue-specific Q distribution. Both APB-coupled Northern blotting and LC–MS/MS analyses revealed that Q is present in all tissues, with heart, skeletal
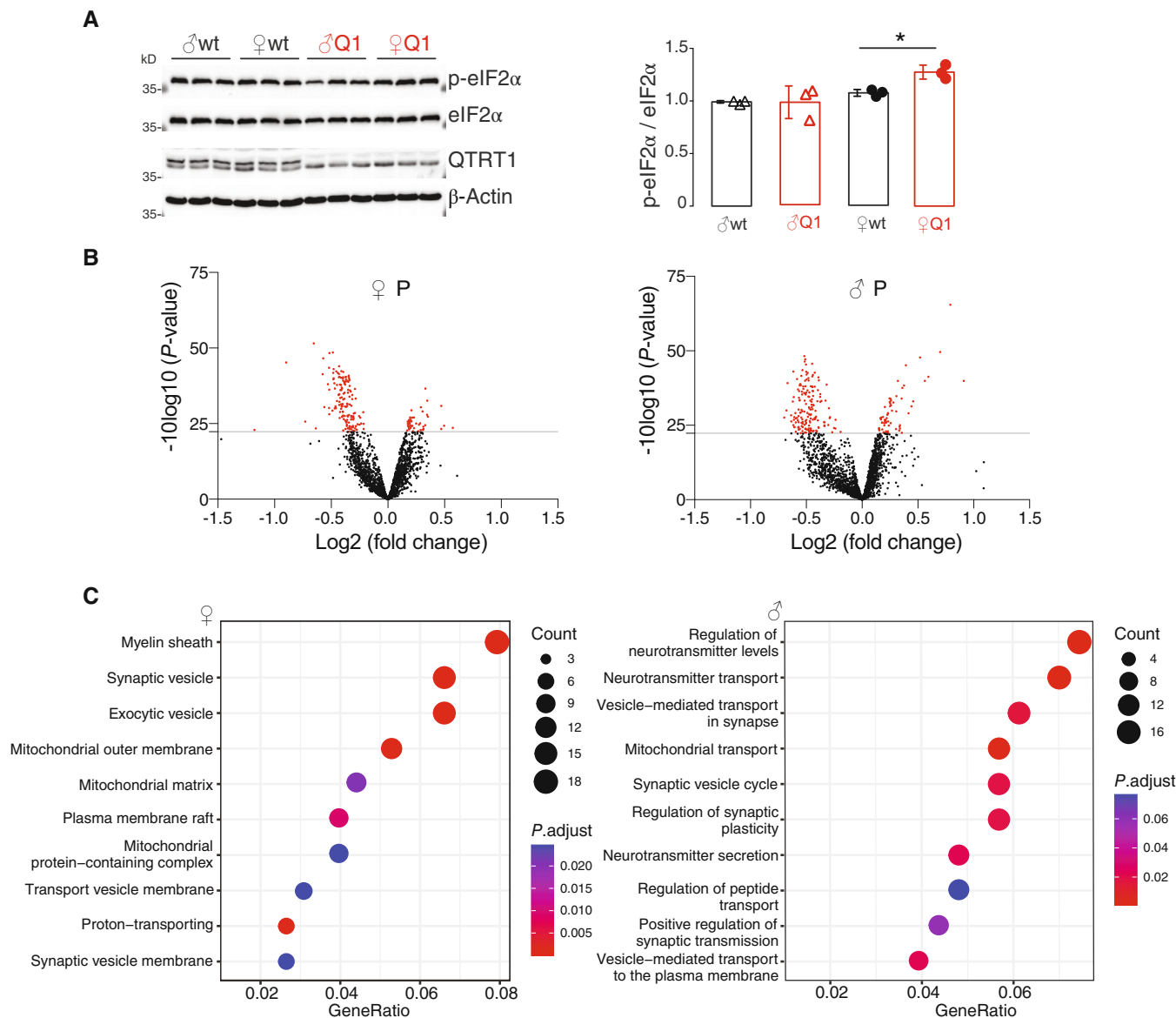
Figure 7. The loss of Q-tRNA modification alters proteome in the adult hippocampus.

A   Western blot analysis showing increased levels of phosphorylated eIF2α upon loss of Q in the 8-month-old female Q1 hippocampi. β-Actin and global eIF2α levels were used as loading controls. Loss of QTRT1 confirms the genotypes. For the quantification of the level of eIF2α phosphorylation, the signal was normalized to total eIF2α. Error bars: ±SD; (n = 6, 3 male and 3 female). *P-value < 0.05, two-tailed unpaired t-test.

B   Dimethyl-labeling analysis of 8-months-old hippocampi. The red dots represent 243 deregulated proteins for male and 188 proteins for female mice. The adjusted P-value < 0.05 is indicated by the horizontal line. n = 6, 3 males and 3 females in 2 technical replicates.

C   Gene ontology analysis of the deregulated proteins. The top 10 biological processes are presented. Adjusted P-value was calculated using Benjamini–Hochberg method.

Data information: P, proteome; Q1, *Qtrt1* knockout mouse; wt, wild-type mouse.
Source data are available online for this figure.

muscle, and brain containing the highest Q levels, whereas spleen has one of the lowest Q-tRNA levels as described previously (Thumbs *et al*, 2020). Even though differences in tissue-specific Q-tRNA content can be explained by differences in tissue turnover rate (Spalding *et al*, 2005), salvage of the micronutrient queuine (Hung *et al*, 2023), and, to some extent, by changes in the expression of the *Qtrt1* gene (Appendix Fig S1D), the molecular mechanism

behind these differences is still not fully explored. One may speculate that an adaptation between Q-tRNA modification level and tissue-specific codon usage, as previously described for *Drosophila* developmental stages (Zaborske *et al*, 2014), may be the driving force.

It has long been postulated that Q plays a critical role in protein translation by influencing tRNA aminoacylation (Singhal &

Vakharia, 1983) or altering codon–anticodon recognition (Meier *et al*, 1985). Our previous findings, however, indicated that nutrition-dependent Q-tRNA modification determines the efficiency and fidelity of translation in both human cancer cell lines and *Schizosaccharomyces pombe* (Tuorto *et al*, 2018; Muller *et al*, 2019). Although the described effects were moderate and species specific, Q was consistently shown to regulate codon-biased translation. To understand the impact of Q on translation, it is helpful to adopt a structure- and energy-based view of the genetic code established by Grosjean and Westhof (2016), who grouped codons into three categories—strong, intermediate, and weak—according to the Turner energies of codon–anticodon binding. While the strong group contains G and/or C in the first two positions of the codon, the weak group contains A and/or U in the first two positions. The codon–anticodon interaction strength is coupled to the speed of decoding since the eviction of near-cognate tRNAs in the ribosomal acceptor site requires a considerable amount of time before a cognate tRNA engages in a productive interaction with the mRNA codon. Hence, weak codons with a higher tRNA dissociation rate should be decoded more rapidly, while strong codons should be decoded more slowly. Unexpectedly, we observed that the loss of Q-tRNA modification not only leads to a reduced speed of translation at Q-decoded codons but also has a systemic effect on the balance of overall translation speed (Fig 5A). While translation of A/U-rich codons was also slowed down in the absence of Q modification, translation of G/C-rich codons was found to be accelerated. This global effect on translation is most likely kinetic, whereby stalling events at the Q-decoded codons cause a slowdown of upstream ribosomes (Fig 5D) primarily on the rapidly decoded weak codons, similar to a traffic jam that has a stronger impact on the fast-moving vehicles.

An imbalance in the speed of codon-biased translation and RQC translational arrest is likely to have a considerable impact on the translatome and translation regulation, giving rise to alterations in the proteome. In agreement with our previous observations in HeLa cells (Tuorto *et al*, 2018), eIF2 signaling, a critical stress-induced regulator of eukaryotic translation (Bhat *et al*, 2015), was deregulated both in the translatome of the Q1 hippocampi and by Western blot (Figs 6C and 7A, and EV5B). In fact, stalling of ribosomes was recently found to cause eIF2α phosphorylation (Wu *et al*, 2020), arguing that stalling at Q-decoded codons in Q1 mice may lead to direct activation of eIF2α signaling. In addition, eIF2α phosphorylation has important functions in brain physiology, beyond its essential role in stress-dependent regulation of translation initiation. Several reports have shown that an increase in eIF2α phosphorylation impairs learning and memory in mice and chicken (Costa-Mattioli *et al*, 2009; Batista *et al*, 2016; Sharma *et al*, 2020), and eIF2α phosphorylation is a common factor in many neurodegenerative diseases (Moon *et al*, 2018). It is conceivable that a permanent imbalance in the speed of decoding leads to chronical translational stress, which may well lead to loss of *Syt1-* and NeuN-expressing neurons and alterations in the dendritic arborization as observed in the Q1 hippocampi (Fig 4). Therefore, exploring the link among Q modification, eIF2 signaling, neurodegeneration, and neurogenesis appears to be a promising avenue for further research.

Finally, it is interesting to note that some microdeletion/microduplication events taking place on the short arm of chromosome 19 in humans (19p13.2), where the *QTRT1* gene is located, have been associated with pathological traits such as autistic-like behavior, anxiety, and intellectual disability (DECIPHER: (Firth *et al*, 2009)). Similarly, microdeletions and microduplications around the *QTRT2* gene have also been linked to neurodevelopmental pathologies including intellectual impairment (DECIPHER: Firth *et al*, 2009). Since the behavioral abnormalities in Q1 mice resemble some of the phenotypic traits of the reported microdeletions/duplications, it will be important to address the possible role of QTRT1 and QTRT2 in neuropsychiatric diseases with impaired learning and memory.

Materials and Methods

Animal handling

All mouse husbandry and related experiments were carried out at the German Cancer Research Center (DKFZ) and at Mannheim Faculty of Medicine, University of Heidelberg, according to applicable laws and regulations. Behavior tests on the other hand were carried out at INBC. Animal experiments (Appendix Table S1) were conducted in strict compliance with national and international guidelines for the Care and Use of Laboratory Animals and were approved by the local government (Regierungspräsidium Karlsruhe, Germany, G64/17, G-102/16, and G-100/16). Behavioral experiments were carried out in compliance with the ARRIVE guidelines. Female mice were not checked for estrous cycle during the experiments. Unless otherwise stated, all animal experiments were conducted blinded and with randomization procedure on adult mice at an age of 3–8 months according to Appendix Table S1.

Cell culture

E14 mouse embryonic stem (mES) cell line (background 129/Ola) was kindly provided by the Transgenic Service, DKFZ, Germany. Cells were grown on mouse embryonic fibroblasts as the feeder layer that were seeded on 0.2% gelatin-coated dishes in knockout DMEM (Gibco) medium supplemented with 10% FBS (Gibco), 1% penicillin/streptomycin (Gibco), 1% glutamax (Gibco), 0.1 mM beta-mercaptoethanol (Sigma- Aldrich), and 1.2×10^3 U LIF (ESGRO). The medium was changed daily and the cells were cultured in 37°C/5% CO_2 incubator and passaged every 2 days.

CRISPR/Cas9 genome editing

The sgRNA (Appendix Fig S2B) was designed using e-CRISP online tool (Heigwer *et al*, 2014) and cloned into lentiCRISPRv1 vector as described previously (Shalem *et al*, 2014). E14 mES cells were transiently transfected with the lentiCRISPRv1-sgRNA plasmid targeting the third exon of *Qtrt1* gene using lipofectamine 3000 (Invitrogen) reagent according to manufacturer's instructions. Editing events resulted in the generation of a heterogeneous cell population that was subjected to up to 5 days of puromycin selection, followed by single clone picking. The nature of the mutations was characterized by Sanger sequencing. Successful heterozygous clones were injected into the blastocyst-stage embryos and Q1 heterozygous progeny was selected and backcrossed for six generations with C57Bl/6J mice, and ultimately, inbred to establish the final homozygous line (Q1; C57BL/6J-*Qtrt1*[em1Tuo]). Putative off-targets were predicted using an

online tool called CCTop (Stemmer *et al*, 2015). The parameters were chosen according to previous studies (Sternberg *et al*, 2014).

RNA isolation

A total of 10^5–10^7 cells, or ~ 50 mg tissue, were homogenized in 1 ml of TRIzol (Invitrogen) and RNA was isolated according to manufacturer's instructions. The RNA concentration and purity were analyzed on NanoDrop (ND-1000) and samples were stored at −80°C.

Northern blotting

Acryloyl aminophenyl boronic acid-based (APB) Northern blotting was performed as described previously (Igloi & Kossel, 1985). Following deacetylation of up to 10 μg of RNA in 100 mM Tris–HCl (pH 9) for 30 min at 37°C, RNA was EtOH precipitated, resuspended in RNA-loading dye (Fermentas), and denatured at 72°C for 3 min prior loading. The gels were run according to our previously published protocol (Cirzi & Tuorto, 2021).

Urea-based Northern blotting was conducted in denaturing conditions. 5 μg of total RNA was resuspended in RNA loading dye (Fermentas) and denatured at 72°C for 3 min. Samples were run on 15% TBE-urea gel (Invitrogen) in TBE buffer at 100 V for 1 h and at 250 V until bromophenol dye reached the end.

All the gels were blotted, hybridized, quantified, and stripped as described previously (Cirzi & Tuorto, 2021).

Northern blot probes: 5′-histidine: CTAACCACTATACGATCACGGC, the probe has full complementary with all histidine tRNAs with the exception of one mismatch with His-GTG-1-1 and His-GTG-3-1.

5′-Asparagine: CTGGGTGGGCTCGAACC, the probe has full complementary with all asparagine tRNAs with the exception of one mismatch with Asn-GTT-1-1 and Asn-GTT-4-1 and Asn-GTT-5-1.

5′-Aspartate: ACCACTATACTAACGAGGA, the probe has full complementary with all aspartate tRNAs.

5′-5S rRNA: GGGTGGTATGGCCGTAGAC.

RNA mass spectrometry

Up to 1500 ng of total RNA was digested to nucleosides and spiked with an internal standard (^{13}C stable isotope-labeled nucleosides from *S. cerevisiae*) as described previously (Freund *et al*, 2019). Afterwards, the samples were subjected to MS analysis as previously described (Vilardo *et al*, 2020). For relative quantification, an internal calibration was applied as indicated in an earlier protocol (Kellner *et al*, 2014).

The MS was operated in the positive ion mode using Agilent MassHunter software in the dynamic MRM (multiple reaction monitoring) mode. For relative quantification, MS/MS signals were normalized to the UV signal of guanosine (G).

Protein extraction

Proteins were extracted from cell pellets or murine hippocampus in lysis buffer containing 25 mM Tris pH 7.5, 27.5 mM NaCl, 25 mM sucrose, 20 mM KCl, 10 mM EDTA, 10 mM EGTA, 1 mM DTT, 10% glycerol, 0.5% NP40, 100 mM NaF, 1 mM Na₃VO₄, 0.04 mM

OA, protease inhibitor cocktail tablet, and phosstop tablet (Roche). Samples were disrupted by passing through a 25G syringe, followed by incubation on ice for 30 min with 10 min vortexing intervals. Protein concentration was determined using Bradford (Bio-Rad) according to manufacturer's instructions.

Western blotting

A 100 μg of denatured protein-loading dye mixtures were run on a 12% SDS–PAGE gel according to standard protocols. Next, the proteins were transferred on a 0.2 mm nitrocellulose membrane in a wet system. All the primary antibodies used were diluted in PBS containing 5% FBS, 2.5% BSA, 0.1% Tween-20, and 0.05% NaN₃ with the exception of anti-QTRT1 and secondary antibodies, which were diluted in 5% skim milk in PBS-0.2% Tween.

Antibodies and appropriate dilutions: rabbit polyclonal anti-QTRT1 antibody (1:1000 dilution) was produced in-house against the human and mouse QTRT1 epitope NWPHNLLTDSGG; anti-EIF2S1 (Abcam ab32157, 1:1000), anti-EIF2 (Enzo ADI-KAP-CP130, 1:1000), anti-RPS3 (Santa Cruz sc-376098, 1:1000 dilution), anti-RPS10 (Abcam ab151550, 1:1000 dilution), anti-RPS20 (Abcam ab133776, 1:1000 dilution), and anti-β-Actin (Santa Cruz sc-47778, 1:1000 dilution).

Open field

An open field of $40 \times 40 \times 40$ cm was used for 10 min under a homogeneously illuminated light source (290 lx) to track the mouse locomotion. All animals were introduced from the same location and movements were recorded and analyzed using SYGNIS tracker v4.1.4. Besides the analysis of the general locomotion, the latency, duration, and the number of visits by the mouse to the inner arena (10×10 cm) in the center of the box were calculated for measuring the anxiety level.

Home cage (LABORAS)

The LABORAS (Laboratory Animal Behavior Observation Registration and Analysis System; Metris BV, Netherlands) was used to detect behavior in a natural home cage environment. Each mouse was tested individually for 24 h in a cage placed on top of the platform under standard housing conditions with free access to food and water. LABORAS software version 2.6 was used to detect and measure vibrations of the animals in cages plated on top of the carbon fiber platform. After recording, climbing, grooming, rearing, locomotion, immobility, and eating and drinking habits were transformed into frequency counts.

Morris water maze

A standard hidden platform protocol (Morris, 1981) was utilized with minor changes. The circular alley ($r = 85$ cm) was filled with opaque water ($21°C \pm 1°C$) until the escape platform ($r = 5$ cm) was 1 cm below the surface. To habituate the mice and measure their visual navigation capability, ample distal cues were placed throughout the maze and the visible platform 1 day before training. The platform was situated once in each of the four quadrants in all four trials. Training consisted of four daily trials over the course of 10 days. To prevent hypothermia, mice were placed under an

infrared lamp after each trial. Each day, animals were introduced to the maze from randomized starting points and led to find the platform for 90 s. Whenever an animal failed to locate the platform during this period, it was directed to the platform by the experimenter and left there for 15 s. One day after the last training day (at day 12), a 120 s probe trial without an escape platform was conducted. In all cases, animals were monitored and analyzed using SYGNIS tracker v4.1.4.

Fear conditioning

The fear conditioning test evaluates natural fear learning. Mice spent 6 min inside a conditioning chamber (Med Associates Inc., St. Albans, Vermont) and were exposed to four conditioned stimuli: acoustic signals (5 kHz, 85 dB, 30 s each) at 90–120, 150–180, 210–240, and 270–300 s. At the last second of each tone segment, an unconditioned stimulus: foot shock (0.6 mA, 1 s) was applied via the floor grid. After 24 h, animals were re-introduced to the chamber for 6 min in the absence of any stimuli to evaluate the contextual fear memory, and after 48 h, the cued fear memory was assessed. During the cue test, the chamber was remodeled with a flat plastic floor panel covering the steel grid and a black roof-shaped insert, and by replacement of visible light with near-infrared illumination and use of source of a perfume. Mice were exposed to this altered context for 4 min during which the 30 s conditioned stimulus was presented twice, terminating at 60 and 180 s, respectively. Freezing behavior was analyzed via a video camera connected to a video tracking software (Med Associates Inc.) to enable measuring the freezing numbers and durations using "Video Freeze" software. The absence of any movement excluding respiration was considered freezing and it was defined by freezing frame as a change in <11 of 76,800 pixels between adjacent frames (33 ms apart) over a time period of >1 s.

IntelliCage

A few days prior to testing, mice were implanted subcutaneously with micro-transponders (Datamars, PetLink, Youngstown, OH, USA) to allow individual animal identification. Groups of five to eight animals per cage of both wt and Q1 genotypes were housed in the IntelliCages and had a habituation period of 3 days with free access to water; during which, the animals were habituated to perform nose pokes to access two water bottles allocated in each of four corners of the cage. This was followed by a 5 days place learning period for which each animal was randomly assigned to one drinking corner, in which a nose poke activated the door giving the mouse access to two water bottles. Next, the animals were assigned to the opposite corner for 3 days reversal learning period. The number of visits as well as nose pokes and licks for each corner were recorded. Animals were observed daily, food was provided *ad libitum* during the experiments, and plastic houses were provided as shelters. Data from the IntelliCages were processed using the IntelliCage software (IntelliCage Plus, 2.4, New Behavior) and only the highest active period, the first 8 h of night (19:30–03.30), was analyzed.

OCT-embedded tissue preparation and cryosection

Immediately *post mortem*, the brain tissue was incubated in fresh 4% PFA with gentle shaking at 4°C for 2 days, followed by 2 days of 30% sucrose incubation for cryopreservation. The tissues were embedded into optimal tissue compound (Tissue-Tek) and frozen directly at −80°C for at least 30 min prior to sectioning and cryosectioned using a CM3050S cryostat (Leica) at 12–14 μm thickness and kept at −20°C ± 1°C.

Nissl staining

Prior to Nissl staining, frozen sections were kept at RT for 1 h and post-fixed with 4% PFA for 10 min. Following standard Nissl staining, slides were mounted with DPX mounting medium (VWR). Pictures were taken with an automated microscope system at 10× magnification (Axio Scan, Zeiss) and processed in ImageJ.

Immunofluorescence and immunohistochemistry

The assays were performed following standard protocols. Briefly: Sections were washed with PBS and blocked with 10% goat serum in PBS-0.01% triton x-100. Following primary and secondary antibody stainings, sections were mounted with a mounting medium containing DAPI (Invitrogen Fluormount-G with DAPI), or alternatively developed using VECTASTAIN ABC Kit (Vector Laboratories). Pictures were taken with SP5 Confocal Microscope (Leica) and an automated microscope system at 40× magnification (Axio Scan, Zeiss). Cells were quantified manually using ImageJ.

Antibodies and appropriate dilutions: anti-GFAP (Thermo Fisher, 13–0300; 1:200 dilution), anti-IBA1 (Fujifilm Wako Chemicals, 019-19741; 1:500 dilution), and anti-NeuN (Millipore, mab377; 1:400 dilution). The number of NeuN-positive nuclei were counted in three sections for each biological replicate in the regions of interest using ImageJ.

DeadEnd Colorimetric TUNEL assay (Promega) was performed according to the manufacturer's instructions.

Chromogenic single *in situ* RNA hybridization

Chromogenic single *in situ* hybridization (ISH) was performed according to previous reports (Schirmer *et al*, 2019) and manufacturer's recommendations (RNAscope 2.5 HD Reagent Kit-RED, ACD Biotechne). Sequences of target probes, amplifier, and label probes are proprietary and commercially available at ACD Biotechne. Following red chromogenic single-molecule *in situ* hybridization to visualize gene expression of *Syt1* and *Plp1* genes expression (ACD Biotechne), hematoxylin and fluorescent DAPI stainings were performed for nucleus counterstaining. Afterwards, sections were mounted with VectaMount Permanent Mounting Medium. As quality control, negative (*DapB*) and positive (*Ppib*, ACD Biotechne) mouse ISH probes were run in parallel. The number of *Plp1*- or *Syt1*-expressing cells was counted manually in the region of interest using ImageJ.

Golgi-Cox staining

Golgi staining was performed using the FD Rapid GolgiStain Kit (FD NeuroTechnologies Inc.) according to manufacturer's recommendations. Granule pyramidal neurons from the DG region were selected for morphological analysis. Dendritic trees were reconstructed using Simple Neurite Tracer (Longair *et al*, 2011) and Sholl analysis was performed using ImageJ. The length of at least 20 dendrites

was measured for each biological replicate in two fields of view and three neurons were reconstructed for each animal analyzed. Dendritic spines were quantified along neurons' secondary shafts by manual counting using ImageJ.

Ribosome profiling

For the library preparation, hippocampi were isolated at 4°C according to Biever *et al* (2020) and Ingolia *et al* (2011)) and directly resuspended in 300 µl polysome lysis buffer containing 20 mM Tris (pH 7.5), 5 mM MgCl$_2$, 150 mM NaCl, 1% Triton X-100, 1 mM DTT, 100 µg/ml cycloheximide, and complete protease inhibitor (Roche). Tissues were homogenized 10 times with a plastic pestle before being pushed through a 25G syringe 10 times. The lysates were cooled on ice for 10 min before being centrifuged at high speed at 4°C for 6 min. After transferring the supernatant to a fresh tube, the centrifugation procedure was repeated. After determining the RNA concentration, 15% of the lysate was utilized as input (see RNA-seq library preparation section) and 20–25% for polysome profiling. Ribosome profiling libraries were prepared using 50% of lysate (Tuorto *et al*, 2018). Sequencing libraries were prepared according to protocol of the NEB NEXT Small RNA Library Prep Set for Illumina (Multiplex Compatible) E7330. Sequencing was performed on a NextSeq 550 platform. Chemistry used: NextSeq 500/550 high-output V2 Kit (75 cycles), FC-404-2005, loaded on FC 1.8 pM. Data analysis was performed using the RiboVIEW pipeline (Legrand & Tuorto, 2020). After adapter removal using cutadapt (v1.8.1), the sequencing reads (26 to 77 million reads per sample) were trimmed with a minimum length of 25 nt and a maximum length of 36 nt, and a quality score of at least 30, using Trimmomatic (v0.39). The remaining reads were depleted of rRNA and other non-coding RNAs by aligning to a depletion reference using Bowtie (v1.0.0). Non-aligned reads in the previous step were finally aligned to the transcriptome (2 to 6 million reads per sample). Both the depletion and the transcriptome reference were downloaded from Ensembl release 101 for *Mus musculus* and processed with custom scripts and gtf2table from RiboVIEW. Footprints that aligned near the start of the annotated sequence were counted to compute periodicity and the coverage was categorized by footprint length and location.

For the codon enrichment (CE), the frequency of codons that appear at any point of the coding sequence was assumed to reflect codon usage. Based on this, unbiased codon enrichment in the A-site and other sites at any offset of the A-site was calculated as the observed codon usage relative to the expected codon usage using Python scripts that are part of RiboVIEW (Legrand & Tuorto, 2020). The observed codon usage was first calculated at mRNA level and second over mRNAs, using weights, defined as the number of reads per mRNA. The expected codon usage was assumed to be independent of the position, except around start and stop codons. The first 15 codons of each ORF were excluded. Standard error was calculated by dividing the standard deviation of codon enrichment by the square root of the number of mRNAs. Single-codon occupancy (SCO) was generated using RiboVIEW (custom script "enrichment.py"). SCO was calculated as the coverage in A-site for a specific codon on a specific mRNA, divided by the expected coverage in the mRNA considered (where expected coverage is the number of reads divided by the number of codons in the coding sequence). SCO is an output of RiboVIEW in

"*.SCO" files, which also contain each codon's raw coverage in the A-site, codon sequence, and percentage of the coding sequence of the mRNA covered by at least one read. Metagenes centered around Q-decoded codons and stratified by A/U-rich and G/C-rich codons were derived from SCO files using a custom R script: for each covered Q-decoded codon position in each covered mRNA, the position 0 was attributed to the Q-decoded codon, and other codons had a relative position to this Q-decoded codon. Raw coverage of each codon was added to the G/C-rich or A/U-rich metagene, depending on codon sequence containing 2 to 3 G or C nucleotides, or 2 to 3 A or U nucleotides, respectively. The metagene is normalized to 1 at the Q-position 0. The comparison was obtained as the means of the set of possible ratios between replicates of one condition versus the other. The standard error of the mean was obtained by taking the standard deviation of the same set. Smoothing was performed using R function loess, with span = 0.2. Since A/U- and G/C-rich codons and weak/strong codons are not independent categories, we left out adjustment for multiple testing.

Polysome profiling

Twenty to 25% of the polysome lysate was subjected to quick polysome profiling analysis. The lysates were ultracentrifuged in a 17.5–50% sucrose gradient using a SW60 rotor at 40,000 rpm (107,328 *g* at top and 205,712 *g* at bottom) for 2 h and the polysome profiles were obtained using a Teledyne Isco fractionator with a sensitivity of 0.5. To calculate the fraction of ribosomes engaged in translation, the area under the polysomal part of the curve was divided by the area below the entire curve.

RNA sequencing

Fifteen percent of polysome lysate was used for RNA-seq library preparation. RNA extraction was performed as described previously (Tuorto *et al*, 2018). After rRNA depletion using Ribo Zero Kit (Illumina), libraries were prepared using NEBNext Ultra II RNA Library Prep Kit (Illumina) according to manufacturer's instructions.

For determining ribosome densities, alignment was performed with bowtie v1.2.2 (Langmead *et al*, 2009) allowing a maximum of two mismatches and reporting all alignments in the best stratum (settings: -a --best --stratum -v 2). Reads that did not map to tRNA or rRNA sequences (as downloaded from the UCSC Genome Browser) were aligned to a mouse transcriptome. Afterwards, reads were summarized at the gene level using samtools v0.1.19 (Li *et al*, 2009) and an in-house developed perl script to count only reads that are between 27 and 30 nt long and map to ORFs of isoforms arising from one specific gene (as defined by a common gene symbol). An offset of 12 nt upstream of the start and stop codon with respect to the 5' end of the reads was assumed. RNA-seq reads were processed in an analogous way, omitting adapter removal and size selection. Finally, 5.4 to 15.5 million reads could be uniquely assigned to genes in each sample.

Ribosome densities were calculated from read counts using DESeq2 v1.30.0 (Love *et al*, 2014) for normalization (applying the median of ratios method) and checking for statistically significant differences between wild-type and Q1 samples (with a likelihood ratio test followed by the Benjamini–Hochberg procedure for multiple testing adjustment).

GC content was calculated as mean of GC content of all isoforms of a gene.

Gene ontology analysis of dysregulated transcripts was performed using PANTHER (Mi *et al*, 2021).

Targeted tRNA bisulfite sequencing

Bisulfite conversion was performed using the EZ RNA Methylation™ Kit (Zymo) using 2 μg of RNA. Following first-strand cDNA synthesis using Superscript III (Invitrogen) and PCR, desired fragments were gel purified. MiSeq amplicons were prepared as described previously (Bormann *et al*, 2019). Data were analyzed using the BisAmp web-based pipeline. Methylation rate was calculated at each position as the fraction of non-converted cytosines.

Proteomics measurement by DML

Freshly isolated hippocampi from female and male mice were lysed in 8 M urea and 50 mM Tris–HCl, pH = 8. The samples were sonicated using an ultrasonic probe (Branson) with three cycles of 10 s pulses at 30% output. After centrifugation at maximum speed (16,000 *g*) in a table-top centrifuge (Eppendorf), the supernatant was transferred to a fresh tube and reduced with 10 mM DTT (Sigma-Aldrich) for 20 min and alkylated using 55 mM iodoacetamide (Sigma-Aldrich) for 30 min in the dark. Afterwards, they were digested using 0.25 μg/μl endo-proteinase LysC (Wako chemicals) for 3 h. The samples were diluted to a final concentration of 1.2 M urea and further digested with 0.25 μg/μl trypsin (Promega) for 16 h at room temperature. The reaction was stopped by adding formic acid to a final concentration of 0.1%. The peptides were desalted on C18 STAGE Tips (Rappsilber *et al*, 2007), and isotope labeled by dimethylation (DML) (Boersema *et al*, 2009). In brief, peptides were resuspended on 20 mM HEPES pH 7,5 to a concentration of 1 mg/ml. We added 4% (v/v) CH_2O (light) for labeling the wild-type (wt) and CD_2O (heavy) for labeling the knockout (Q1) in both male and female mice and 0.1 M $NaBH_3CN$ as a catalysator. The samples were incubated at 21°C for 90 min. After a second C18 desalting, the samples were resuspended in 0.1% formic acid and analyzed by mass spectrometry.

All samples were analyzed on an Ultimate3000 nanoHPLC system (Dionex) coupled to a Q-Exactive HF mass spectrometer (Thermo Fisher Scientific), equipped with a nanoelectrospray source. Peptides were separated on a C_{18} Acclaim™ 15-cm analytical column (Thermo Fisher Scientific). We used 130 min gradient and 190 min gradient for the technical replicates at a flow rate of 300 nl/min ramping from 2 to 35% buffer B (90% ACN and 0.1% formic acid). The mass spectrometer was operated in DDA mode to automatically isolate and fragment the top 12 multiple-charged precursors at 70,000 resolution and 3 × 10e6 AGC, with 90 ms of injection time (IT) at MS level, scanning from 350 to 1,500 Th in profile mode. The isolation window was set to 2 Th. For MS/MS, 17,500 resolution and 1 × 10e5 AGC, with 45 ms of IT, were chosen. All raw LC–MS/MS data were processed with MaxQuant (Cox & Mann, 2008) v2.0.1.0 using the Andromeda search engine and searched against the complete human UniProt database (UP000005640, downloaded 2021–04). In addition, the default contaminant protein database was included. The SILAC re-quantify (REQ) features were activated where indicated. Three biological

replicates were measured for female and male hippocampus cells in two technical replicates. Carbamidomethylation of cysteines was specified as a fixed modification for all groups. Variable modifications considered were oxidation of methionine and protein N-terminal acetylation. The DML labeled modification was set as standard multiplicity 2. Quantification data of labeled peptides were measured considering N-termini and lysine dimethylation on light (+28 Da) or heavy (+32 Da) modification per free primary amine. False discovery rate (FDR) filtering was set to 1% on peptide spectrum match (PSM), PTM site, and protein level. For further data analysis, we used specialized using custom R scripts with R 64-bit version 4.1.0, and the shiny package Protigy (https://github.com/broadinstitute/protigy). We analyzed the DML experiments by moderated one-sample *t*-test. Adjusted *P*-value < 0.05 (Benjamini–Hochberg correction) was used as a threshold value for the cut-off (wt vs. Q1). Dataset EV2 contains all the results from analysis. Missing values were replaced by random numbers drawn from a normal distribution with a width of 0.3 and a down shift of 1.8 using Perseus software (v1.6.7.0) (Tyanova *et al*, 2016). Gene ontology analysis of dysregulated proteins was performed using R-based programming with clusterprofiler package (Wu *et al*, 2021a).

Statistical procedures

Data were analyzed using GraphPad Prism 8 software. Unpaired student's *t*-test was used to assess differences between two groups, and two-way analysis of variance (ANOVA) tests followed by Benjamini and Hochberg *post hoc* test were used to examine time point measurements. Wilcoxon rank-sum tests and beta regression were performed with R. For comparing percentages, we used the R package betareg (Cribari-Neto & Zeileis, 2010). For analyzing the effect of *Qtrt1* knockout in male and female mice separately, the regression model contained time and genotype (~ time + genotype). When the effect of sex on the genotype differences was analyzed, we included an interaction term (~ time + genotype + sex + sex: genotype). A two-tailed *P*-value of 0.05 was considered significant unless specified. Data are presented as means ± SE, ± SEM or ± SD.

Data availability

Gene expression and ribosome profiling sequencing data are available in the NCBI GEO database: GSE180766 (http://www.ncbi.nlm.nih.gov/geo/query/acc.cgi?acc=GSE180766; Dataset EV1). The mass spectrometry proteomics data have been deposited to the ProteomeXchange Consortium via the MassIVE database with the dataset identifier PXD034504 (Dataset EV2).

Expanded View for this article is available online.

Author contributions

Cansu Cirzi: Conceptualization; data curation; formal analysis; validation; investigation; visualization; methodology; writing – original draft; writing – review and editing. **Julia Dyckow:** Data curation; formal analysis; validation; investigation; visualization; methodology; writing – original draft. **Carine Legrand:** Software; formal analysis; validation; investigation; visualization; methodology; writing – original draft. **Johanna Schott:** Data curation; software; formal analysis; validation; investigation; visualization; methodology; writing – original draft. **Wei Guo:** Data curation; formal analysis; validation; investigation; visualization; methodology. **Daniel Perez Hernandez:** Data curation; software; formal analysis; validation; investigation; visualization; methodology. **Miharu Hisaoka:** Formal analysis; investigation; visualization; methodology. **Rosanna Parlato:** Conceptualization; supervision; investigation; visualization; methodology; writing – original draft; writing – review and editing. **Claudia Pitzer:** Supervision; methodology. **Franciscus van der Hoeven:** Resources; methodology. **Gunnar Dittmar:** Resources; supervision; funding acquisition; methodology. **Mark Helm:** Resources; supervision; funding acquisition; methodology. **Georg Stoecklin:** Conceptualization; resources; supervision; funding acquisition; visualization; writing – original draft; writing – review and editing. **Lucas Schirmer:** Supervision; funding acquisition; methodology; writing – original draft. **Frank Lyko:** Conceptualization; resources; supervision; funding acquisition; writing – original draft. **Francesca Tuorto:** Conceptualization; resources; data curation; software; formal analysis; supervision; funding acquisition; investigation; visualization; methodology; writing – original draft; project administration; writing – review and editing.

Disclosure and competing interests statement

The authors declare that they have no conflict of interest.

References

Agris PF, Eruysal ER, Narendran A, Väre VYP, Vangaveti S, Ranganathan SV (2017) Celebrating wobble decoding: Half a century and still much is new. *RNA Biol* 15: 537–553

Batista G, Johnson JL, Dominguez E, Costa-Mattioli M, Pena JL (2016) Translational control of auditory imprinting and structural plasticity by eIF2alpha. *eLife* 5: e17197

Bednarova A, Hanna M, Durham I, VanCleave T, England A, Chaudhuri A, Krishnan N (2017) Lost in translation: defects in transfer RNA modifications and neurological disorders. *Front Mol Neurosci* 10: 135

Beier H, Barciszewska M, Sickinger HD (1984) The molecular basis for the differential translation of TMV RNA in tobacco protoplasts and wheat germ extracts. *EMBO J* 3: 1091–1096

Benavides-Piccione R, Regalado-Reyes M, Fernaud-Espinosa I, Kastanauskaite A, Tapia-Gonzalez S, Leon-Espinosa G, Rojo C, Insausti R, Segev I, DeFelipe J (2020) Differential structure of hippocampal CA1 pyramidal neurons in the human and mouse. *Cereb Cortex* 30: 730–752

Bhat M, Robichaud N, Hulea L, Sonenberg N, Pelletier J, Topisirovic I (2015) Targeting the translation machinery in cancer. *Nat Rev Drug Discov* 14: 261–278

Biever A, Glock C, Tushev G, Ciirdaeva E, Dalmay T, Langer JD, Schuman EM (2020) Monosomes actively translate synaptic mRNAs in neuronal processes. *Science* 367: eaay4991

Boersema PJ, Raijmakers R, Lemeer S, Mohammed S, Heck AJ (2009) Multiplex peptide stable isotope dimethyl labeling for quantitative proteomics. *Nat Protoc* 4: 484–494

Boland C, Hayes P, Santa-Maria I, Nishimura S, Kelly VP (2009) Queuosine formation in eukaryotic tRNA occurs via a mitochondria-localized heteromeric transglycosylase. *J Biol Chem* 284: 18218–18227

Bolnick DI, Snowberg LK, Hirsch PE, Lauber CL, Org E, Parks B, Lusis AJ, Knight R, Caporaso JG, Svanback R (2014) Individual diet has sex-dependent effects on vertebrate gut microbiota. *Nat Commun* 5: 4500

Bormann F, Tuorto F, Cirzi C, Lyko F, Legrand C (2019) BisAMP: a web-based pipeline for targeted RNA cytosine-5 methylation analysis. *Methods* 156: 121–127

Brule CE, Grayhack EJ (2017) Synonymous codons: choose wisely for expression. *Trends Genet* 33: 283–297

Cirzi C, Tuorto F (2021) Analysis of queuosine tRNA modification using APB northern blot assay. *Methods Mol Biol* 2298: 217–230

Conti L, Del Corno M, Gessani S (2020) Revisiting the impact of lifestyle on colorectal cancer risk in a gender perspective. *Crit Rev Oncol Hematol* 145: 102834

Costa A, Païs de Barros J-P, Keith G, Baranowski W, Desgrès J (2004) Determination of queuosine derivatives by reverse-phase liquid chromatography for the hypomodification study of Q-bearing tRNAs from various mammal liver cells. *J Chromatogr B* 801: 237–247

Costa-Mattioli M, Sossin WS, Klann E, Sonenberg N (2009) Translational control of long-lasting synaptic plasticity and memory. *Neuron* 61: 10–26

Cowan CSM, Cryan JF (2021) The microbiome-gut-brain axis in neurocognitive development and decline. *Mod Trends Psychiatry* 32: 12–25

Cox J, Mann M (2008) MaxQuant enables high peptide identification rates, individualized p.p.b.-range mass accuracies and proteome-wide protein quantification. *Nat Biotechnol* 26: 1367–1372

Cribari-Neto F, Zeileis A (2010) Beta regression in R. *J Stat Softw* 34: 1–24

Crick FH (1966) Codon—anticodon pairing: the wobble hypothesis. *J Mol Biol* 19: 548–555

Cryan JF, O'Riordan KJ, Cowan CSM, Sandhu KV, Bastiaanssen TFS, Boehme M, Codagnone MG, Cussotto S, Fulling C, Golubeva AV *et al* (2019) The microbiota-gut-brain axis. *Physiol Rev* 99: 1877–2013

Duechler M, Leszczynska G, Sochacka E, Nawrot B (2016) Nucleoside modifications in the regulation of gene expression: focus on tRNA. *Cell Mol Life Sci* 73: 3075–3095

Ehrenhofer-Murray AE (2017) Cross-talk between Dnmt2-dependent tRNA methylation and queuosine modification. *Biomolecules* 7: 14

Fergus C, Barnes D, Alqasem MA, Kelly VP (2015) The queuine micronutrient: charting a course from microbe to man. *Nutrients* 7: 2897–2929

Fergus C, Al-Qasem M, Cotter M, McDonnell CM, Sorrentino E, Chevot F, Hokamp K, Senge MO, Southern JM, Connon SJ *et al* (2021) The human tRNA-guanine transglycosylase displays promiscuous nucleobase preference but strict tRNA specificity. *Nucleic Acids Res* 49: 4877–4890

Fernandez-Chacon R, Konigstorfer A, Gerber SH, Garcia J, Matos MF, Stevens CF, Brose N, Rizo J, Rosenmund C, Sudhof TC (2001) Synaptotagmin I functions as a calcium regulator of release probability. *Nature* 410: 41–49

Firth HV, Richards SM, Bevan AP, Clayton S, Corpas M, Rajan D, Van Vooren S, Moreau Y, Pettett RM, Carter NP (2009) DECIPHER: database of

chromosomal imbalance and phenotype in humans using ensembl resources. *Am J Hum Genet* 84: 524–533

Freund I, Buhl DK, Boutin S, Kotter A, Pichot F, Marchand V, Vierbuchen T, Heine H, Motorin Y, Helm M *et al* (2019) 2'-O-methylation within prokaryotic and eukaryotic tRNA inhibits innate immune activation by endosomal toll-like receptors but does not affect recognition of whole organisms. *RNA* 25: 869–880

Gaur R, Bjork GR, Tuck S, Varshney U (2007) Diet-dependent depletion of queuosine in tRNAs in *Caenorhabditis elegans* does not lead to a developmental block. *J Biosci* 32: 747–754

Grosjean H, Westhof E (2016) An integrated, structure- and energy-based view of the genetic code. *Nucleic Acids Res* 44: 8020–8040

Gusel'nikova VV, Korzhevskiy DE (2015) NeuN as a neuronal nuclear antigen and neuron differentiation marker. *Acta Naturae* 7: 42–47

Hainmueller T, Bartos M (2020) Dentate gyrus circuits for encoding, retrieval and discrimination of episodic memories. *Nat Rev Neurosci* 21: 153–168

Han L, Phizicky EM (2018) A rationale for tRNA modification circuits in the anticodon loop. *RNA* 24: 1277–1284

Heigwer F, Kerr G, Boutros M (2014) E-CRISP: fast CRISPR target site identification. *Nat Methods* 11: 122–123

Homma D, Katoh S, Tokuoka H, Ichinose H (2013) The role of tetrahydrobiopterin and catecholamines in the developmental regulation of tyrosine hydroxylase level in the brain. *J Neurochem* 126: 70–81

Hou YM, Gamper H, Yang W (2015) Post-transcriptional modifications to tRNA—a response to the genetic code degeneracy. *RNA* 21: 642–644

Hung SH, Elliott GI, Ramkumar TR, Burtnyak L, McGrenaghan CJ, Alkuzweny S, Quaiyum S, Iwata-Reuyl D, Pan X, Green BD *et al* (2023) Structural basis of Qng1-mediated salvage of the micronutrient queuine from queuosine-5'-monophosphate as the biological substrate. *Nucleic Acids Res* 51: 935–951

Igloi GL, Kossel H (1985) Affinity electrophoresis for monitoring terminal phosphorylation and the presence of queuosine in RNA. Application of polyacrylamide containing a covalently bound boronic acid. *Nucleic Acids Res* 13: 6881–6898

Ingolia NT, Ghaemmaghami S, Newman JR, Weissman JS (2009) Genome-wide analysis in vivo of translation with nucleotide resolution using ribosome profiling. *Science* 324: 218–223

Ingolia NT, Lareau LF, Weissman JS (2011) Ribosome profiling of mouse embryonic stem cells reveals the complexity and dynamics of mammalian proteomes. *Cell* 147: 789–802

Ishimura R, Nagy G, Dotu I, Chuang JH, Ackerman SL (2016) Activation of GCN2 kinase by ribosome stalling links translation elongation with translation initiation. *Elife* 5: e14295

Jackson D, Kirkbride J, Croudace T, Morgan C, Boydell J, Errazuriz A, Murray RM, Jones PB (2013) Meta-analytic approaches to determine gender differences in the age-incidence characteristics of schizophrenia and related psychoses. *Int J Methods Psychiatr Res* 22: 36–45

Kang HJ, Park Y, Yoo KH, Kim KT, Kim ES, Kim JW, Kim SW, Shin IS, Yoon JS, Kim JH *et al* (2020) Sex differences in the genetic architecture of depression. *Sci Rep* 10: 9927

Katze JR, Basile B, McCloskey JA (1982) Queuine, a modified base incorporated posttranscriptionally into eukaryotic transfer RNA: wide distribution in nature. *Science* 216: 55–56

Kellner S, Ochel A, Thuring K, Spenkuch F, Neumann J, Sharma S, Entian KD, Schneider D, Helm M (2014) Absolute and relative quantification of RNA modifications via biosynthetic isotopomers. *Nucleic Acids Res* 42: e142

Kirtland GM, Morris TD, Moore PH, O'Brian JJ, Edmonds CG, McCloskey JA, Katze JR (1988) Novel salvage of queuine from queuosine and absence of

queuine synthesis in Chlorella pyrenoidosa and Chlamydomonas reinhardtii. *J Bacteriol* 170: 5633–5641

Kiryk A, Janusz A, Zglinicki B, Turkes E, Knapska E, Konopka W, Lipp HP, Kaczmarek L (2020) IntelliCage as a tool for measuring mouse behavior—20 years perspective. *Behav Brain Res* 388: 112620

Langmead B, Trapnell C, Pop M, Salzberg SL (2009) Ultrafast and memory-efficient alignment of short DNA sequences to the human genome. *Genome Biol* 10: R25

Legrand C, Tuorto F (2020) RiboVIEW: a computational framework for visualization, quality control and statistical analysis of ribosome profiling data. *Nucleic Acids Res* 48: e7

Lehmann J, Libchaber A (2008) Degeneracy of the genetic code and stability of the base pair at the second position of the anticodon. *RNA* 14: 1264–1269

Li H, Handsaker B, Wysoker A, Fennell T, Ruan J, Homer N, Marth G, Abecasis G, Durbin R, Genome Project Data Processing S (2009) The Sequence alignment/map format and SAMtools. *Bioinformatics* 25: 2078–2079

Li KK, Concepcion RY, Lee H, Cardinal BJ, Ebbeck V, Woekel E, Readdy RT (2012) An examination of sex differences in relation to the eating habits and nutrient intakes of university students. *J Nutr Educ Behav* 44: 246–250

Longair MH, Baker DA, Armstrong JD (2011) Simple Neurite Tracer: open source software for reconstruction, visualization and analysis of neuronal processes. *Bioinformatics* 27: 2453–2454

Love MI, Huber W, Anders S (2014) Moderated estimation of fold change and dispersion for RNA-seq data with DESeq2. *Genome Biol* 15: 550

Manickam N, Joshi K, Bhatt MJ, Farabaugh PJ (2016) Effects of tRNA modification on translational accuracy depend on intrinsic codon-anticodon strength. *Nucleic Acids Res* 44: 1871–1881

Meier F, Suter B, Grosjean H, Keith G, Kubli E (1985) Queuosine modification of the wobble base in tRNAHis influences 'in vivo' decoding properties. *EMBO J* 4: 823–827

Mendrek A, Mancini-Marie A (2016) Sex/gender differences in the brain and cognition in schizophrenia. *Neurosci Biobehav Rev* 67: 57–78

Mi H, Ebert D, Muruganujan A, Mills C, Albou LP, Mushayamaha T, Thomas PD (2021) PANTHER version 16: a revised family classification, tree-based classification tool, enhancer regions and extensive API. *Nucleic Acids Res* 49: D394–D403

Moon SL, Sonenberg N, Parker R (2018) Neuronal regulation of eIF2alpha function in health and neurological disorders. *Trends Mol Med* 24: 575–589

Morris RGM (1981) Spatial localization does not require the presence of local cues. *Learn Motiv* 12: 239–260

Muller M, Hartmann M, Schuster I, Bender S, Thuring KL, Helm M, Katze JR, Nellen W, Lyko F, Ehrenhofer-Murray AE (2015) Dynamic modulation of Dnmt2-dependent tRNA methylation by the micronutrient queuine. *Nucleic Acids Res* 43: 10952–10962

Muller M, Legrand C, Tuorto F, Kelly VP, Atlasi Y, Lyko F, Ehrenhofer-Murray AE (2019) Queuine links translational control in eukaryotes to a micronutrient from bacteria. *Nucleic Acids Res* 47: 3711–3727

Nagaraja S, Cai MW, Sun J, Varet H, Sarid L, Trebicz-Geffen M, Shaulov Y, Mazumdar M, Legendre R, Coppee JY *et al* (2021) Queuine is a nutritional regulator of entamoeba histolytica response to oxidative stress and a virulence attenuator. *mBio* 12: e03549-20

Nishimura S (1983) Structure, biosynthesis, and function of queuosine in transfer RNA. *Prog Nucleic Acid Res Mol Biol* 28: 49–73

Ogle JM, Carter AP, Ramakrishnan V (2003) Insights into the decoding mechanism from recent ribosome structures. *Trends Biochem Sci* 28: 259–266

Orton SM, Herrera BM, Yee IM, Valdar W, Ramagopalan SV, Sadovnick AD, Ebers GC, Canadian Collaborative Study Group (2006) Sex ratio of multiple sclerosis in Canada: a longitudinal study. *Lancet Neurol* 5: 932–936

Papaleo F, Erickson L, Liu G, Chen J, Weinberger DR (2012) Effects of sex and COMT genotype on environmentally modulated cognitive control in mice. *Proc Natl Acad Sci USA* 109: 20160–20165

Rakovich T, Boland C, Bernstein I, Chikwana VM, Iwata-Reuyl D, Kelly VP (2011) Queuosine deficiency in eukaryotes compromises tyrosine production through increased tetrahydrobiopterin oxidation. *J Biol Chem* 286: 19354–19363

Rappsilber J, Mann M, Ishihama Y (2007) Protocol for micro-purification, enrichment, pre-fractionation and storage of peptides for proteomics using StageTips. *Nat Protoc* 2: 1896–1906

Reyniers JP, Pleasants JR, Wostmann BS, Katze JR, Farkas WR (1981) Administration of exogenous queuine is essential for the biosynthesis of the queuosine-containing transfer RNAs in the mouse. *J Biol Chem* 256: 11591–11594

Richard P, Kozlowski L, Guillorit H, Garnier P, McKnight NC, Danchin A, Maniere X (2021) Queuine, a bacterial-derived hypermodified nucleobase, shows protection in in vitro models of neurodegeneration. *PloS One* 16: e0253216

Ruitenberg MFL, van Wouwe NC, Wylie SA, Abrahamse EL (2021) The role of dopamine in action control: insights from medication effects in Parkinson's disease. *Neurosci Biobehav Rev* 127: 158–170

Schirmer L, Velmeshev D, Holmqvist S, Kaufmann M, Werneburg S, Jung D, Vistnes S, Stockley JH, Young A, Steindel M *et al* (2019) Neuronal vulnerability and multilineage diversity in multiple sclerosis. *Nature* 573: 75–82

Sebastiani M, Behrens C, Dorr S, Gerber HD, Benazza R, Hernandez-Alba O, Cianferani S, Klebe G, Heine A, Reuter K (2022) Structural and biochemical investigation of the heterodimeric murine tRNA-guanine transglycosylase. *ACS Chem Biol* 17: 2229–2247

Shalem O, Sanjana NE, Hartenian E, Shi X, Scott DA, Mikkelson T, Heckl D, Ebert BL, Root DE, Doench JG *et al* (2014) Genome-scale CRISPR-Cas9 knockout screening in human cells. *Science* 343: 84–87

Sharma V, Sood R, Khlaifia A, Eslamizade MJ, Hung TY, Lou D, Asgarihafshejani A, Lalzar M, Kiniry SJ, Stokes MP *et al* (2020) eIF2alpha controls memory consolidation via excitatory and somatostatin neurons. *Nature* 586: 412–416

Siard TJ, Jacobson KB, Farkas WR (1991) Queuine metabolism and cadmium toxicity in *Drosophila melanogaster*. *Biofactors* 3: 41–47

Singhal RP, Vakharia VN (1983) The role of queuine in the aminoacylation of mammalian aspartate transfer RNAs. *Nucleic Acids Res* 11: 4257–4272

Singhal RP, Kopper RA, Nishimura S, Shindo-Okada N (1981) Modification of guanine to queuine in transfer RNAs during development and aging. *Biochem Biophys Res Commun* 99: 120–126

Skolnick SD, Greig NH (2019) Microbes and monoamines: potential neuropsychiatric consequences of dysbiosis. *Trends Neurosci* 42: 151–163

Slobodin O, Davidovitch M (2019) Gender differences in objective and subjective measures of ADHD among clinic-referred children. *Front Hum Neurosci* 13: 441

Snyder HM, Asthana S, Bain L, Brinton R, Craft S, Dubal DB, Espeland MA, Gatz M, Mielke MM, Raber J *et al* (2016) Sex biology contributions to vulnerability to Alzheimer's disease: a think tank convened by the Women's Alzheimer's Research Initiative. *Alzheimers Dement* 12: 1186–1196

Spalding KL, Bhardwaj RD, Buchholz BA, Druid H, Frisen J (2005) Retrospective birth dating of cells in humans. *Cell* 122: 133–143

Stemmer M, Thumberger T, Del Sol KM, Wittbrodt J, Mateo JL (2015) CCTop: an intuitive, flexible and reliable CRISPR/Cas9 target prediction tool. *PloS One* 10: e0124633

Sternberg SH, Redding S, Jinek M, Greene EC, Doudna JA (2014) DNA interrogation by the CRISPR RNA-guided endonuclease Cas9. *Nature* 507: 62–67

Suzuki T, Suzuki T (2014) A complete landscape of post-transcriptional modifications in mammalian mitochondrial tRNAs. *Nucleic Acids Res* 42: 7346–7357

Thumbs P, Ensfelder TT, Hillmeier M, Wagner M, Heiss M, Scheel C, Schon A, Muller M, Michalakis S, Kellner S *et al* (2020) Synthesis of galactosyl-queuosine and distribution of hypermodified Q-nucleosides in mouse tissues. *Angew Chem Int Ed Engl* 59: 12352–12356

Tucker LB, Fu AH, McCabe JT (2016) Performance of male and female C57BL/6J mice on motor and cognitive tasks commonly used in pre-clinical traumatic brain injury research. *J Neurotrauma* 33: 880–894

Tuorto F, Legrand C, Cirzi C, Federico G, Liebers R, Muller M, Ehrenhofer-Murray AE, Dittmar G, Grone HJ, Lyko F (2018) Queuosine-modified tRNAs confer nutritional control of protein translation. *EMBO J* 37: e99777

Tyanova S, Temu T, Sinitcyn P, Carlson A, Hein MY, Geiger T, Mann M, Cox J (2016) The Perseus computational platform for comprehensive analysis of (prote)omics data. *Nat Methods* 13: 731–740

Varghese S, Cotter M, Chevot F, Fergus C, Cunningham C, Mills KH, Connon SJ, Southern JM, Kelly VP (2017) *In vivo* modification of tRNA with an artificial nucleobase leads to full disease remission in an animal model of multiple sclerosis. *Nucleic Acids Res* 45: 2029–2039

Vilardo E, Amman F, Toth U, Kotter A, Helm M, Rossmanith W (2020) Functional characterization of the human tRNA methyltransferases TRMT10A and TRMT10B. *Nucleic Acids Res* 48: 6157–6169

Werling DM (2016) The role of sex-differential biology in risk for autism spectrum disorder. *Biol Sex Differ* 7: 58

Wu CC, Peterson A, Zinshteyn B, Regot S, Green R (2020) Ribosome collisions trigger general stress responses to regulate cell fate. *Cell* 182: 404–416.e4

Wu T, Hu E, Xu S, Chen M, Guo P, Dai Z, Feng T, Zhou L, Tang W, Zhan L *et al* (2021a) clusterProfiler 4.0: a universal enrichment tool for interpreting omics data. *Innovation* 2: 100141

Wu WL, Adame MD, Liou CW, Barlow JT, Lai TT, Sharon G, Schretter CE, Needham BD, Wang MI, Tang W *et al* (2021b) Microbiota regulate social behaviour via stress response neurons in the brain. *Nature* 595: 409–414

Zaborske JM, DuMont VL, Wallace EW, Pan T, Aquadro CF, Drummond DA (2014) A nutrient-driven tRNA modification alters translational fidelity and genome-wide protein coding across an animal genus. *PLoS Biol* 12: e1002015